PSFC/JA-13-50

External excitation of a short-wavelength fluctuation in the Alcator C-Mod edge plasma and its relationship to the Quasi-Coherent Mode

T. Golfinopoulos, B. LaBombard, R.R. Parker, W. Burke, E. Davis, R. Granetz, M. Greenwald, J. Irby, R. Leccacorrvi, E. Marmar, W. Parkin, M. Porkolab, J. Terry, R. Vieira, S. Wolfe, and the Alcator C-Mod team

March, 2014

Plasma Science and Fusion Center
Massachusetts Institute of Technology
Cambridge MA 02139 USA

This work was supported by the U.S. Department of Energy Cooperative Agreement DE-FC02-99ER54512.

Submitted for publication in *Physics of Plasmas*.

External excitation of a short-wavelength fluctuation in the Alcator C-Mod edge plasma and its relationship to the Quasi-Coherent Mode

T. Golfinopoulos, B. LaBombard, R.R. Parker, W. Burke, E. Davis, R. Granetz, M. Greenwald, J. Irby, R. Leccacorvi, E. Marmar, W. Parkin, M. Porkolab, J. Terry, R. Vieira, S. Wolfe, and the Alcator C-Mod team

Plasma Science and Fusion Center, Massachusetts Institute of Technology, Cambridge, MA 02139

(Dated: 19 March 2014)

A novel "Shoelace" antenna has been used to inductively excite a short-wavelength edge fluctuation in a tokamak boundary layer for the first time. The principal design parameters, $k_\perp = 1.5 \pm 0.1$ cm^{-1} and $45 < f < 300$ kHz, match the Quasi-Coherent Mode (QCM, $k_\perp \sim 1.5$ cm^{-1}, $f \sim 50 - 150$ kHz) in Alcator C-Mod, responsible for exhausting impurities in the steady-state, ELM-free Enhanced D_α (EDA) H-mode. In H-mode, whether or not there is a QCM, the antenna drives coherent, field-aligned perturbations in density, $\tilde{n}_e$, and field, $\tilde{B}_\theta$, which are guided by field lines, propagate in the electron diamagnetic drift direction, and exhibit a weakly-damped ($\gamma/\omega_0 \sim 5 - 10\%$) resonance near the natural QCM frequency. This result is significant, offering the possibility that externally-driven modes may be used to enhance particle transport. In L-mode, the antenna drives only a non-resonant $\tilde{B}_\theta$ response. The facts that the driven mode has the same wave number and propagation direction as the QCM, and is resonant at the QCM frequency, suggest the antenna may couple to this mode, which we have shown elsewhere to be predominantly drift-mode-like (B. LaBombard *et al.*, Phys. Plasmas 2014-accepted).

PACS numbers: 52.25.Fi, 52.30.-q, 52.35.-g, 52.35.Ra, 52.40.Fd, 52.55.Fa

I. INTRODUCTION

A unifying observation across virtually all steady-state, high-confinement fusion plasma regimes is the critical role played by edge fluctuations in regulating transport across the plasma boundary. On the Alcator C-Mod tokamak, two instances of this phenomenon are offered by the Enhanced D_α (EDA) H-mode[1] - which features a Quasi-Coherent Mode (QCM, $f = 50{-}150$ kHz, $k_\perp = 1.5$ cm^{-1}) - and the Improved Energy Confinement Regime (I-Mode)[2] - associated with the Weakly Coherent Mode (WCM, $f = 100 - 500$ kHz, $k_\perp = 1.5$ cm^{-1}). Examples from other devices include the Quiescent H-mode first observed on the DIII-D tokamak[3], the High Recycling Steady (HRS) H-mode seen on the JFT-2M tokamak[4], and the High-Density H-mode (HDH) found on the W7-AS stellarator[5]. The Quiescent H-mode features the Edge Harmonic Oscillation, while the HRS H-mode features Low- and High-Frequency quasi-coherent modes, and the HDH is accompanied by its own quasi-coherent mode.

The prevalence of these coherent edge structures across such a vast range of parameter space, the critical role they play in sustaining high confinement operation, and the fact that they all have a strong poloidal magnetic field signature inspired us to ask the question: can we directly couple to and/or interact with these modes using an antenna? In so doing, could we actively probe the physics of the target edge fluctuation, affect or actively drive edge transport, destabilize edge modes and trigger a confinement transition, or impart a torque to the plasma?

The present work documents our attempt to answer these questions using a purpose-built, inductive excitation structure, the "Shoelace antenna," on Alcator C-Mod. The paper is organized as follows: in Section II, we provide a brief overview of the characteristics of the QCM, to which the antenna was designed to couple, and review previous experiments which have been successful in coupling to and driving relevant plasma modes. Section III introduces the Shoelace antenna apparatus, describes the arrangement of key diagnostics, and outlines the experimental program. Section IV then describes the edge fluctuations produced by the antenna in the initial round of experiments; of principal importance is the finding that, in H-mode plasmas, the antenna drives fluctuations of similar character to the intrinsic QCM, which display a resonance around the QCM center frequency and appear whether or not an intrinsic QCM is present. Finally, in Section V, we summarize our

conclusions and outline directions for future experimental and computational investigations.

II. BACKGROUND

A. The EDA Regime and the Quasi Coherent Mode

The Enhanced D_α (EDA) H-mode[1,6–11] is a steady-state, high-confinement regime without ELMs that is readily produced on the Alcator C-Mod tokamak[12] (R=0.68 m, $B_t \leq 8$ T, $\bar{n}_e \lesssim 4 \times 10^{20}$ m^{-3}). It features a continuous edge fluctuation, the Quasi-Coherent Mode (QCM), which is responsible for exhausting particles through the plasma boundary, regulating the pedestal. The reduction in particle confinement relative to ELM-free H-mode is accompanied by an increase in D_α emission, motivating the name of the regime. However, the energy confinement time is only slightly reduced, and is comparable to the level achieved in ELMy H-mode.

Recent measurements[11] with a reciprocating Mirror Langmuir Probe scanning through the mode layer have revealed the QCM to be an electron drift wave that further displays both interchange and electromagnetic physics, spans the last closed flux surface in a narrow (∼3 mm) layer, and shows strong fluctuation amplitudes, with $\Delta n_e/\bar{n}_e$ ∼30% and $\Delta T_e/\bar{T}_e \sim e\Delta\tilde{\Phi}/T_e \sim 40\%$, and (from scanning Mirnov coil data) $\tilde{B}_r/B_\theta \sim 0.1\%$. Moreover, measurements of the particle flux driven by the QCM corroborate earlier investigations that ascribe to the QCM the role of exhausting particles from the plasma in the EDA regime. The importance of drift waves and drift-Alfvénic turbulence[13–25] in controlling the C-Mod edge plasma state had already been revealed[26], but their association with the QCM is only recently established. Several experimental characterizations of the QCM[8,10,11,27,28], including the most recent, have described a narrow edge mode having $50 \lesssim f \lesssim 150$ kHz and $k_\perp \sim 1.5$ cm^{-1} at the midplane, approximately field-aligned with $k_\perp \gg k_\parallel$, absent from the high-field side, and with large amplitude fluctuations.

Figure 1 shows representative spectrograms from the phase contrast imaging (PCI) diagnostic sensitive to line-averaged electron density fluctuations, $\tilde{\bar{n}}_e$, as well as a Mirnov coil measuring $\tilde{B}_\theta$, from a discharge with an EDA H-mode. Several parameter traces are also shown. Early in the discharge, the confinement transitions from L-mode to ELM-free H-mode, but the reduction in particle transport is accompanied by a build-up of impurities,

indicated by a strongly-increasing radiated power signal. This leads to a back-transition to L-Mode. Shortly afterward, the plasma again transitions to H-mode, but now, a continuous fluctuation develops - the QCM - visible in the PCI spectrogram as the narrow feature sweeping down in frequency before modulating around a stable average value. The rise of both radiated power and density is arrested, while the D_α light increases, indicating an increase in particle transport that provides a defining characteristic of the EDA regime.

B. External Excitation of Plasma Modes

The importance of edge fluctuations in controlling edge transport has prompted a number of experiments attempting to interact with these modes. Uckan *et al.* employed electrostatic launching probes on the Texas Experimental Tokamak (TEXT), together with a feedback system, and found that they were able to suppress or promote broadband edge turbulence depending on the phase delay in the feedback circuit[29]. Similar results were found by Zhai *et al.* on the KT-5C tokamak after reproducing the experimental setup from TEXT, with the additional observation that, for a particular phase delay, a quasi-coherent mode accompanied the suppression of broadband turbulence[30]. Work on linear devices by Schröder *et al.*[31] and Brandt *et al.*[32,33] employed a set of eight probes arranged azimuthally around the plasma column. They demonstrated open loop control resulting in both suppression of broadband drift wave turbulence, with decreased turbulence-driven transport, and nonlinear interaction with coherent drift waves. They also found that a mode- and frequency-selective (spatiotemporal) excitation structure was essential to coupling to drift waves, as was driving parallel currents with the same structure as the intrinsic mode.

In addition to probes, inductive structures have also been used to stimulate edge activity, as in the study by Borg *et al.* on the TORTUS tokamak[34]. There, a single-winding dipole antenna was employed with the goal of driving shear Alfvén modes in the plasma edge. The antenna winding could be rotated arbitrarily with respect to the equilibrium magnetic field; it was found that the maximum response was achieved when the winding was exactly aligned with the background field, and also that the driven mode was strongly guided by the field lines. Brandt *et al.* also complemented their electrostatic probe exciter with an inductive setup using eight saddle coils, arranged azimuthally around, and external to, the plasma[33]. The saddle coils reproduced the same open-loop control of drift waves as the electrostatic

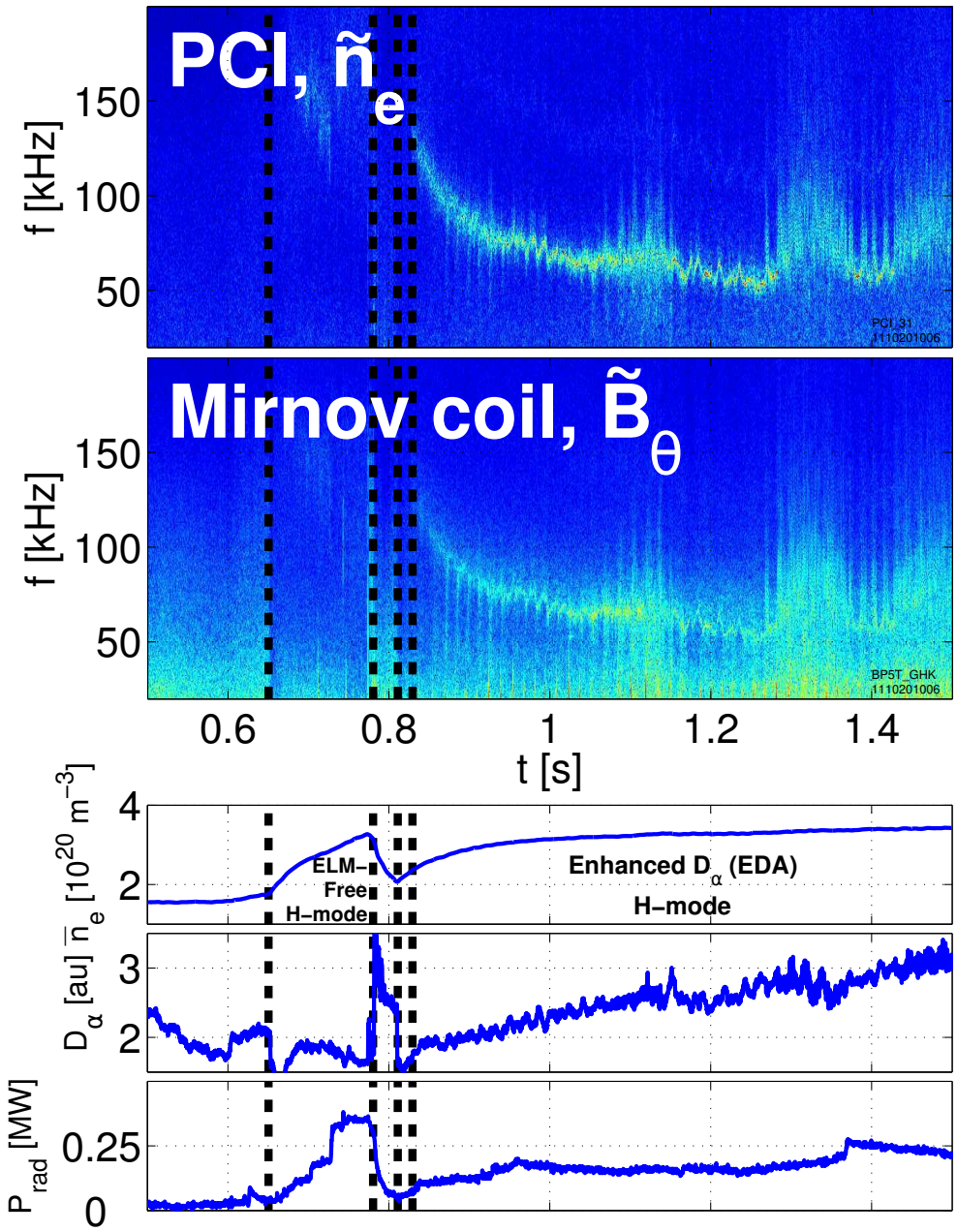

FIG. 1: Spectrograms of phase contrast imaging (PCI, $\tilde{\bar{n}}_e$) and Mirnov coil ($\tilde{B}_\theta$) fluctuation signals, together with line-averaged density ($\bar{n}_e$), D_α, and radiated power (P_{rad}) traces, from a discharge exhibiting both ELM-free and EDA H-modes. The reduced particle confinement of the EDA H-mode relative to the prior ELM-free H-mode is indicated both by the slower density rise and increased D_α light.

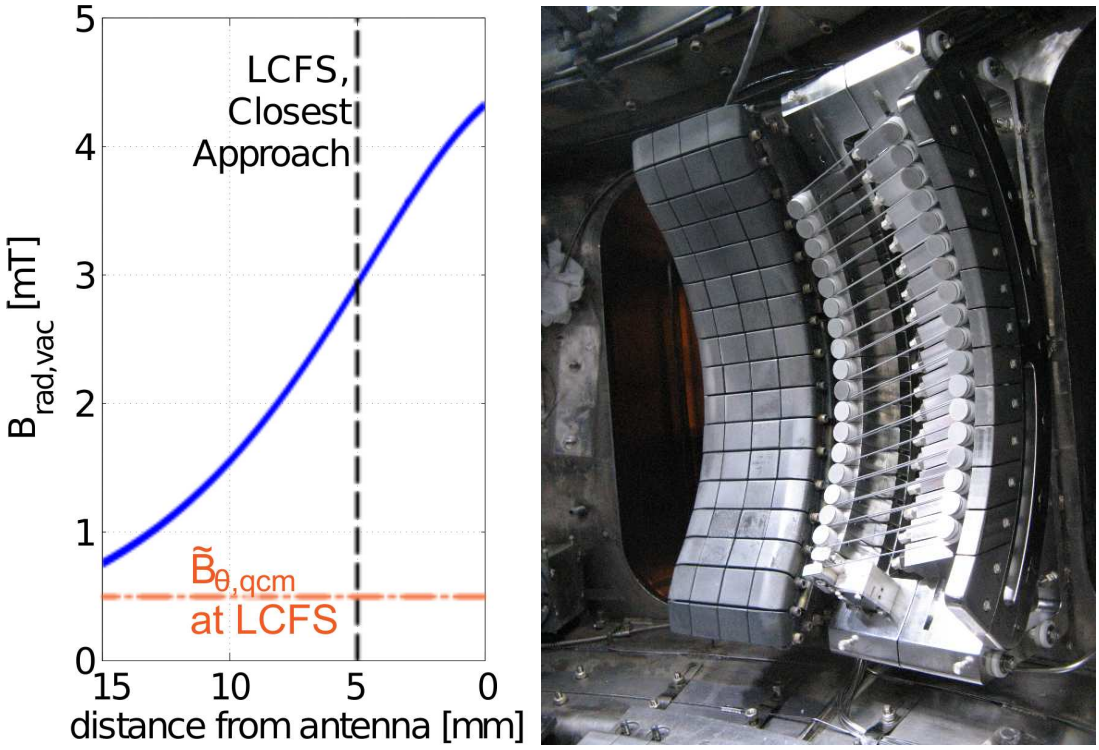

(a) (b)

FIG. 2: (a) Approximate radial vacuum field produced by the antenna; also shown are the LCFS at closest possible approach, as well as the nominal $\tilde{B}_\theta$ amplitude of the QCM. (b) Photograph of the Shoelace antenna mounted inside the Alcator C-Mod vacuum vessel.

probes.

There have also been many attempts to excite specific plasma modes - typically Alfvénic - in order to characterize their physics. Such work falls under the category of Active MHD (AMHD) spectroscopy, which typically seeks additionally to diagnose a plasma based on the driven response. Initial proposals for AMHD spectroscopy were made by Goedbloed *et al.*[35], with pioneering experimental investigation carried out on the Joint European Torus[36–40] using both direct inductive and parametric drive. Similar AMHD experiments were performed on Alcator C-Mod[41–44], finding broadly comparable results.

III. EXPERIMENTAL SETUP

A. The Shoelace Antenna

The Shoelace antenna is wound from a single length of 1.5 mm-diameter lanthanum-doped molybdenum wire (Plansee "ML" wire, 0.3% La_2O_3 by weight[45]). The winding is in two layers, with the wire criss-crossing its way up the ceramic (alumina) tension wheels in 19 rungs, and then retracing its path again on the top layer so as to reinforce the current from the bottom layer. The wire path gives the impression of a shoelace, from which the antenna takes its name. The interlayer spacing is 4.6 mm, only slightly less than the distance between the top layer and the LCFS at the point of closest approach. This is significant since the fall-off of the vacuum field perturbation is rapid, dropping roughly exponentially on the length scale of twice the spacing between rungs (e.g. $2\pi/k_\perp$)[46].

Figure 2 shows a photograph of the antenna mounted in the Alcator C-Mod vacuum vessel, together with a plot of the approximate vacuum field, last closed flux surface (LCFS) location, and nominal QCM $\tilde{B}_\theta$ amplitude.

The wires are field-aligned when the safety factor at the 95% flux surface, q_{95}, is 3, the same value used in the discharges of the earlier characterization of the QCM by Snipes *et al.*[8] The perpendicular spacing is $\Delta z_\perp = 2.1$ cm, giving $k_\perp = \pm 1.5 \pm 0.1$ cm^{-1}, with the spread corresponding to the full-width at half maximum (FWHM) of the $k_\perp$ spectrum calculated from the finite extent of the antenna in the perpendicular direction (e.g. (19 rungs$-1)\times\Delta z_\perp$). Since the antenna wires are angled at $\theta_w = 14.5°$, the Shoelace antenna's toroidal mode number, n, spectrum is centered on $n_0 = 2\pi R_0/\left[2\Delta z_\perp/\tan(\theta_w)\right] \approx 35$, where $R_0 = 0.916$ m is the major radius of the top layer Shoelace rung at the midplane. The bandwidth of the n spectrum is limited by the width of the antenna, $w = 15.3$ cm; modeling the antenna as a tophat function in toroidal angle, ϕ, with an arc length of w gives a factor of sinc $\left(\frac{nw}{2R}\right)$ in the transform, or a span of $\Delta n \approx \pm 23$ from n_0 (FWHM). These values ensure good coupling to the QCM, which typically has[8] $k_\perp = 1.5$ cm^{-1} and $n = 10 - 25$ (at higher safety factor), as well as to the WCM, which has a similar $k_\perp$ and n spectrum[2,47]. It should be noted that the antenna has *no preferred direction*; it produces an RF vacuum field which is a standing wave in the (ϕ, θ) directions and decays rapidly in the radial dimension.

In a single poloidal cross section, the rungs of the antenna on the top layer fall on a circle

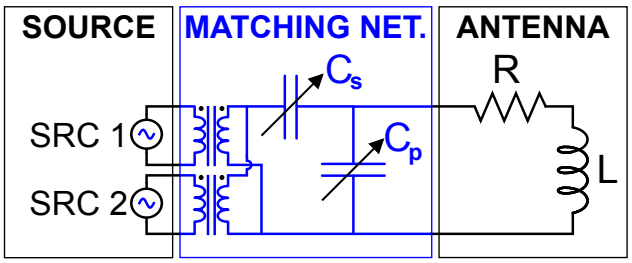

FIG. 3: L-match network, dynamically tunable in real-time in response to changing frequency, used to couple two commercial, 50-Ω T&C AG1010 amplifiers to the Shoelace antenna, which presents a low-impedance, inductive load.

centered at $R = 0.613$ m, $z = 0$ m, with a radius of 0.303 m. At closest approach, the rungs can be as little as 5 mm behind the LCFS. This proximity is required to maximize the induced perturbation in the plasma given its rapid radial decay; however, it also risks damage to the antenna due to the large heat flux in the C-Mod edge. As seen in Figure 2, the antenna is sandwiched between and in the shadow of the main limiter as well as a smaller protection limiter. These provide a degree of shielding. Nonetheless, careful experimental planning, as well as a robust design of the Shoelace support structure, were needed to extend the longevity of the antenna in the harsh C-Mod edge environment.

The Shoelace power system will be described elsewhere[48]. However, a brief overview is given here. The Shoelace antenna operates in a broad band from 45-300 kHz, covering the QCM frequency range (50-150 kHz), as well as part of the WCM band (120-500 kHz). A custom matching network, described schematically in Figure 3, couples power from two 1-kW T&C AG1010 50-Ω amplifiers to the low-impedance, inductive antenna. The matching network uses solid-state switching to discretely tune the system to the drive frequency in real time, and provides excellent performance across the entire operational band. This is demonstrated in Figure 4, which shows power transmission into the matching network, current driven in the antenna, and combined power output from the two amplifiers from an antenna test. At frequencies within the QCM band of these experiments (typically 80-120 kHz), about 1600 W or better of the available 2 kW is dissipated in the antenna.

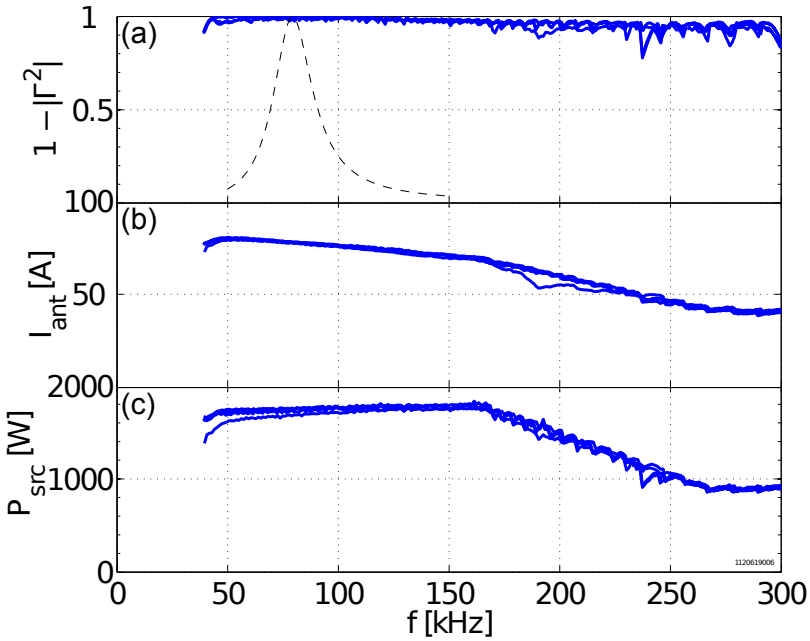

FIG. 4: Matching network performance from a single discharge with two upward and two downward frequency scans from 40 to 300 kHz. (a) Fraction of power transmitted into *matching network*; dashed black line also shows modeled throughput expected from a frequency scan using a single switching state. (b) Current throughput into antenna. (c) Combined source power output from two amplifiers.

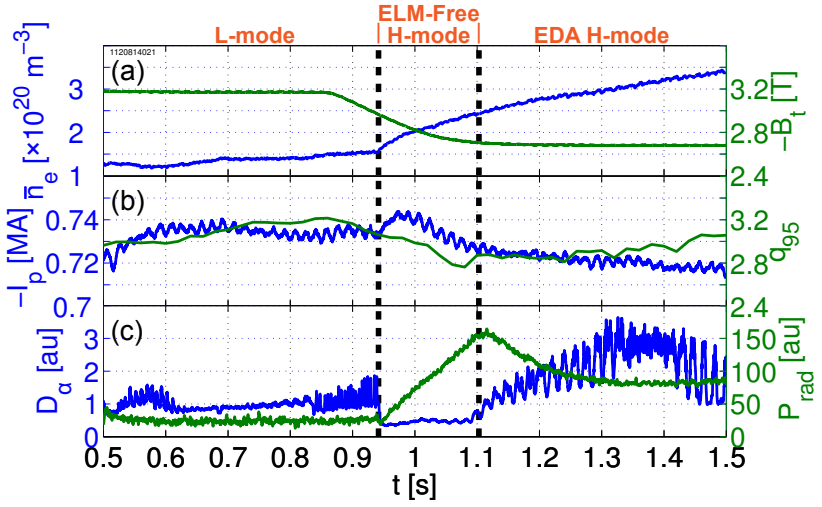

FIG. 5: Traces of (a) line averaged electron density (left axis) and toroidal field (right axis), (b) plasma current (left axis) and safety factor at 95% flux surface (right axis), and (c) D_α light (left axis) and radiated power (right axis) for a typical forward-field discharge.

B. Discharge Development

Discharge parameters from the Shoelace experimental campaign approximated those used in the earlier examination of the QCM by Snipes *et al.*[8], since the Shoelace antenna was designed based upon the characterization of the QCM provided by this study. This choice was additionally motivated by the need to reduce the gap between plasma and antenna, as described above. The low-heating-power ohmic EDA H-modes achieved in these target discharges help to avoid damaging the winding given its proximity to the plasma.

Traces from a typical discharge are shown in Figure 5. Transition to H-mode was facilitated by ramping down the toroidal field to reduce the threshold heating power. Since EDA H-modes tend to favor higher q_{95}[1], it was expected that this parameter would have to be subsequently ramped up after the transition to ELM-free H-mode; in practice, this was not necessary, and q_{95} was maintained near the value that optimized the alignment between the Shoelace winding and the equilibrium field.

The edge region of several ohmic EDA H-modes used in Shoelace antenna experiments was well-diagnosed by the Mirror Langmuir Probe (MLP), and its properties are discussed in detail elsewhere[11]. The MLP revealed that the LCFS in these discharges is typified by $T_e \approx 50$ eV and $n_e \approx 1.5 \times 10^{20}$ m^{-3}, so that $\tau_{ei} \approx 100$ ns and $\tau_{ii} \approx 5$ μs, with $k_\perp \rho_s \approx 0.07$ for the antenna-imposed wave number.

C. Diagnostic Setup

Figure 6 shows a plan view (R, ϕ) of Alcator C-Mod, and indicates the placement of the Shoelace antenna relative to a number of fluctuation diagnostics; a (ϕ, z) view is shown in Figure 7, together with several poloidal cross sections of key diagnostics. Shown also are field lines along the last closed flux surface; these connect to the positions on the LCFS to which the antenna rungs project along rays to the antenna arc center. The following section reveals that, in fact, the antenna-driven fluctuation is guided by field lines, such that diagnostics which do not map to the antenna on a field line near the LCFS do not observe the driven mode. The diagnostics which are almost always mapped to the antenna include phase contrast imaging[49] (PCI), measuring line averaged density fluctuations, $\tilde{\bar{n}}_e$, with 32 vertical chords in a poloidal cross section having a uniform spacing, ΔR =2.7 mm, in major radius;

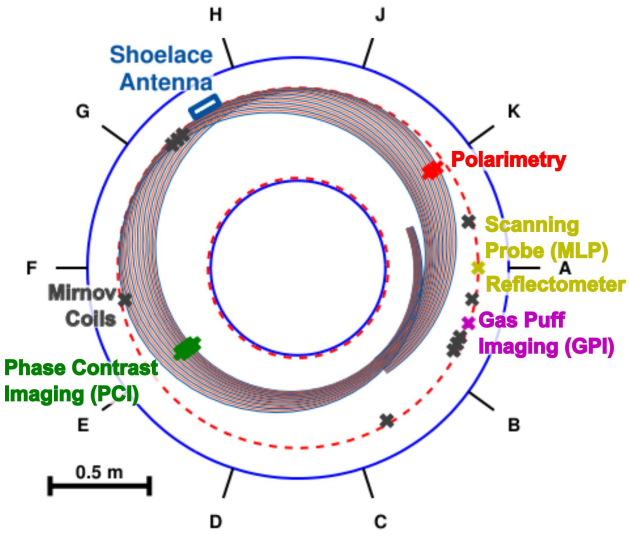

FIG. 6: Plan view (R, ϕ) of Alcator C-Mod tokamak indicating locations of Shoelace antenna and fluctuation diagnostic measurements on the LCFS. Also plotted are magnetic field lines on the LCFS which map to rungs on the Shoelace antenna. Adjacent field lines alternate in color between blue and orange. The 10 equispaced horizontal ports are labeled A-K (skipping the letter, I).

three polarimetry[50] chords, sensitive to both density and magnetic field fluctuations (though in the present work, the contribution from $\tilde{\mathbf{B}}$ is negligible); and wall-mounted Mirnov coils[43], measuring $\tilde{B}_\theta$. The reflectometer, scanning Mirror Langmuir Probe, and gas puff imaging diagnostics do not map to the antenna.

IV. RESULTS AND DISCUSSION

A. Antenna in Receiver Mode

Before discussing the results obtained from energizing the antenna, it is interesting to examine the voltage induced across the antenna by the fluctuating radial magnetic field associated with the QCM. Figure 8 shows a spectrogram of the short-time magnitude squared coherence, $|P_{xy}/\sqrt{P_{xx}P_{yy}}|^2$, with P_{xy} the cross power spectral density between signals, x and y, between this induced voltage and the signal from a PCI chord measuring $\tilde{\tilde{n}}_e$; the high degree of coherence illustrates that the antenna, when used as a receiver highly selective in $k_\perp$, is sensitive to the QCM. The presence of a strong induced signal across the eighteen

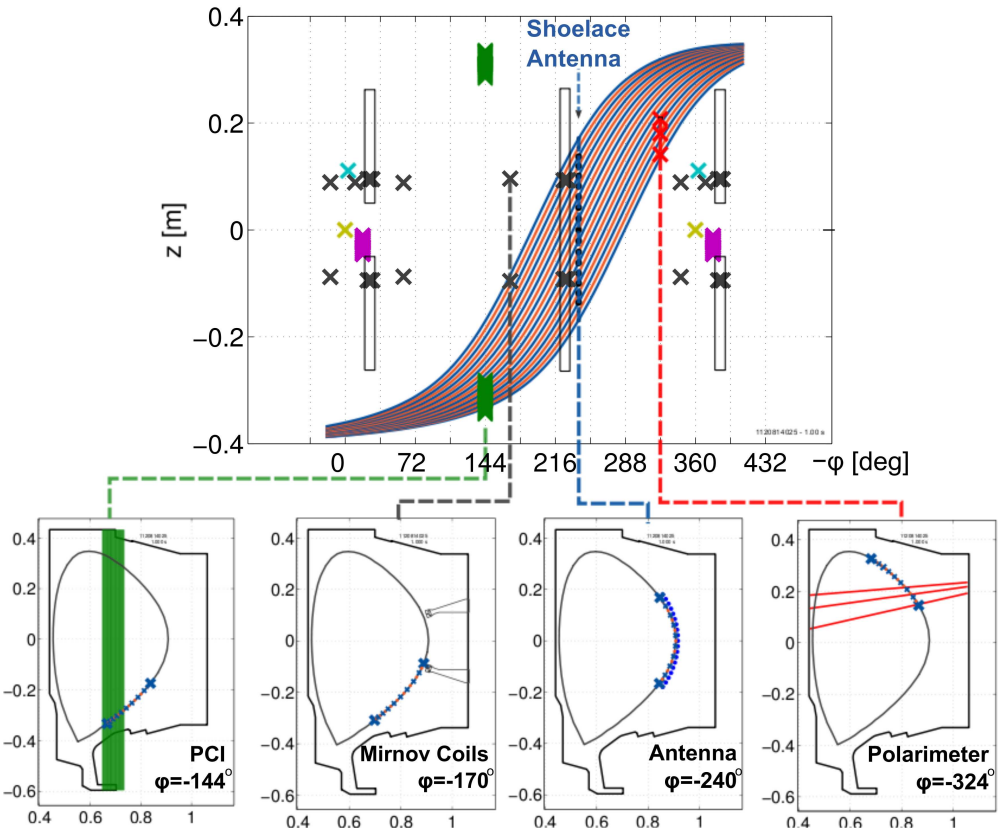

FIG. 7: Field-line mapping projected onto (ϕ, z) plane, showing diagnostic projections onto the LCFS ($\times$'s), as well as Shoelace rungs ($\bullet$'s) and limiters (boxes). Diagnostics and limiters are repeated as the view wraps around past 360°(toroidal). Breakout plots underneath are (R, z) cross-sections; units on axes are in meters.

dipole loops of the antenna also indicates that the QCM has a long poloidal correlation length.

B. Antenna in Driver Mode

Figure 9a shows spectrograms from a PCI chord, a polarimeter chord, and a Mirnov coil, as well as $\bar{n}_e$ and D_α traces, from a discharge in which the Shoelace antenna was driven. Additional traces from this discharge are shown in Figure 5. A dashed line indicates the transition between ohmic L- and ohmic H-mode. A brief ELM-free H-mode gives way to an EDA H-mode, with a QCM visible in the spectra of all three diagnostics, and, after a short delay, an accompanying rise in D_α, consistent with a reduction in particle confinement.

Also visible in the spectrograms of all three diagnostics is a triangular waveform which

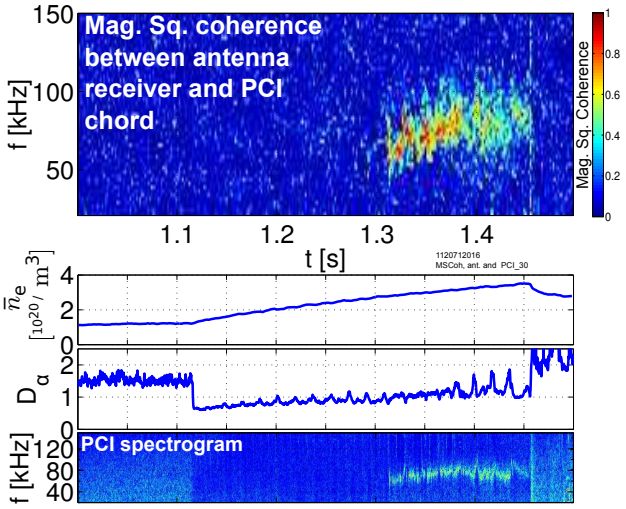

FIG. 8: Short-time ($\sim$ 3.3 ms bins) magnitude squared coherence spectra between voltage induced over Shoelace antenna and PCI fluctuation signal showing that the Shoelace antenna can pick up the QCM fluctuation.

precisely tracks the Shoelace antenna drive frequency. Several observations are noteworthy: (a) a $\tilde{B}_\theta$ perturbation at the antenna frequency is visible in both ohmic L- and H-mode, while the driven $\tilde{n}_e$ fluctuation only appears in H-mode; (b) the driven fluctuation appears strongest near the QCM center frequency, but is also present away from this frequency; (c) the driven $\tilde{n}_e$ appears early in the ELM-free H-mode phase, slightly preceding the QCM. These remarks are true in general for the perturbation driven by the Shoelace antenna.

A clearer view of the driven perturbation is offered by examining the magnitude squared coherence between the antenna current signal, I_a, and the fluctuation diagnostic signals, u, $|P_{I_a u}/\sqrt{P_{I_a I_a} P_{uu}}|^2$, computed over a short, running time window that spans about 3.3 ms. This short-time magnitude squared coherence is shown for the same three fluctuation signals in Figure 9b. We see now that the coherent perturbation in the PCI signal appears immediately after the transition to ELM-free H-mode, while a coherent $\tilde{B}_\theta$ signal is present throughout the entire Shoelace pulse.

Another feature of the driven perturbation is that it is not global. Rather, it is guided by field lines which map to antenna rungs. Figure 10 illustrates this point. Here, a poloidal cross section is shown which contains two Mirnov coils sitting on extensions from the vacuum vessel wall. The LCFS is also reproduced, together with the Shoelace antenna rung positions projected onto the LCFS and mapped to this toroidal location on field lines. Both

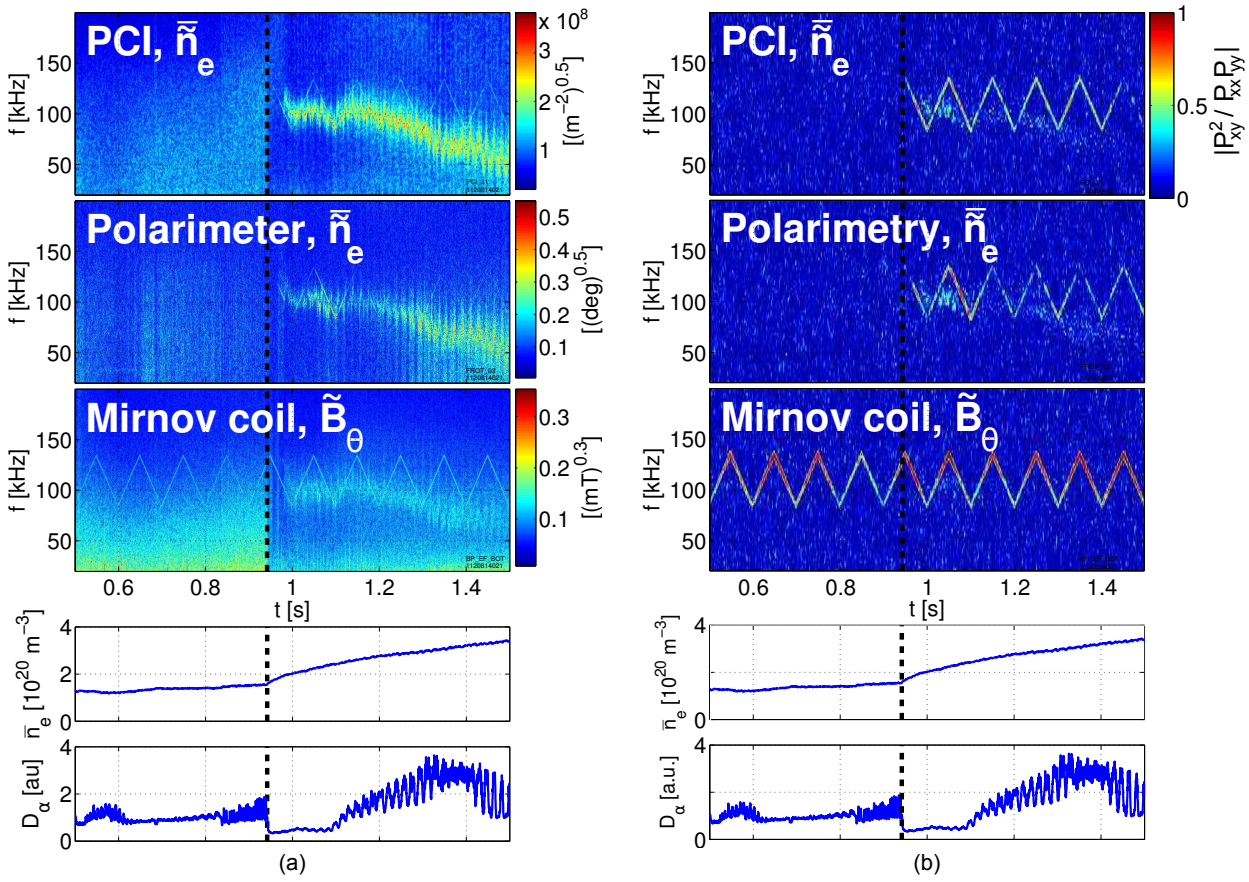

FIG. 9: (a) Spectrograms of fluctuations signals from a PCI chord, a polarimeter chord, and a Mirnov coil during a discharge in which the Shoelace antenna was energized, together with density and D_α traces. The Shoelace response is seen in the triangle-wave feature in the spectrograms, which tracks the drive frequency and appears on top of the intrinsic QCM fluctuation. The spectral amplitudes are raised by an exponent to aid in visualizing the Shoelace response. The [deg] abbreviation in the polarimetry panel refers to degrees of Faraday rotation. The Mirnov coil measurement is given at the coil. The vertical dashed line marks the transition between L- and H-mode. (b) Short-time ($\sim$ 3.3 ms bins) magnitude squared coherence between the antenna current and PCI, Mirnov coil, and polarimeter fluctuation signals. The $\bar{n}_e$ and D_α traces are reproduced.

coils pick up the QCM. However, while the bottom coil, which does map to the Shoelace antenna, shows strong cross coherence with the antenna current throughout the duration of the discharge, the top coil, which does not map to the antenna, has very little cross-coherence.

It should be pointed out that the Mirnov coils do not provide a point-localized measurement, and neither do the PCI or polarimetry chords. This complicates the mapping

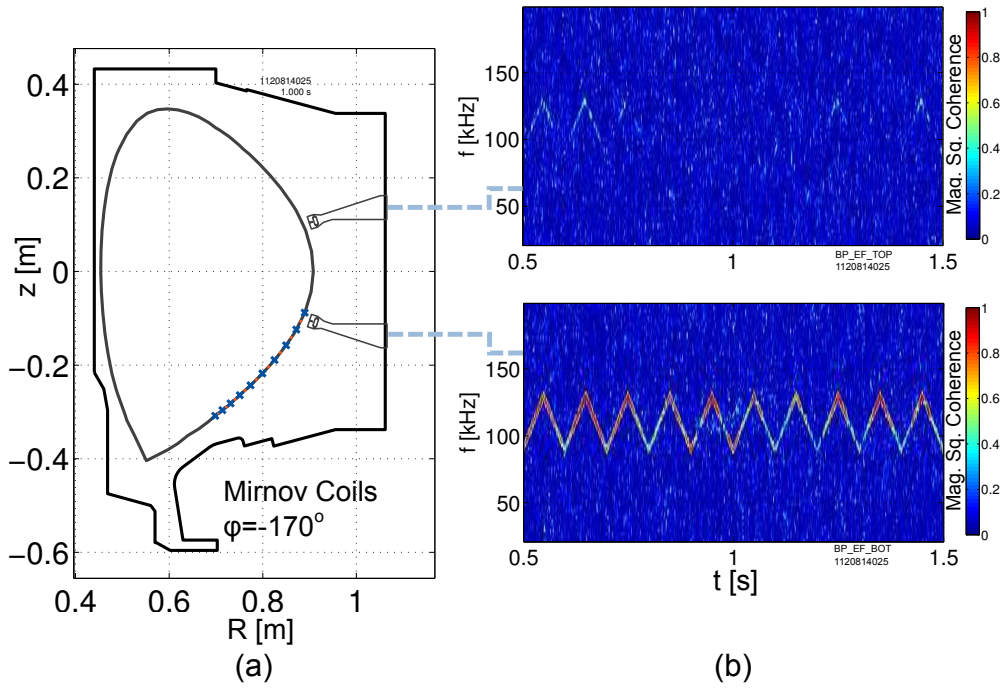

FIG. 10: (a) Cross section showing location of two Mirnov coils, mounted on standoffs from the vacuum vessel, the LCFS (solid black line), and field lines (×'s and •'s) mapping Shoelace rungs on LCFS. (b) Short-time magnitude squared coherence for each coil; strong coherent response on bottom coil, almost none on top.

analysis, and also leads to uncertainty in the mode location. It has been assumed here and elsewhere in this work that the driven mode is localized to a narrow layer around the LCFS. This assumption is inspired by the recent measurements made with the Mirror Langmuir Probe (MLP)[11] described earlier, which show that the QCM, itself, is localized within a ~ 3 mm layer spanning the LCFS. Moreover, the rapid-fall-off of the antenna vacuum field, and the experimental requirement of minimizing the gap between antenna and plasma in order to observe a strong driven response, limits the radial extent in which we expect to find the driven mode to the edge plasma. Nonetheless, at present, we have not measured precisely where the mode envelope is localized radially; such measurements will be carried out using the MLP. However, because the field-line mapping between the antenna and these diagnostics remains sufficiently far from the single x-point, so that magnetic shear remains low on the field line path, the results shown below pertaining to field-line mapping are robust against this uncertainty in the mode flux surface. We will return to this topic in the discussion of wave number estimates, Sec. IV C.

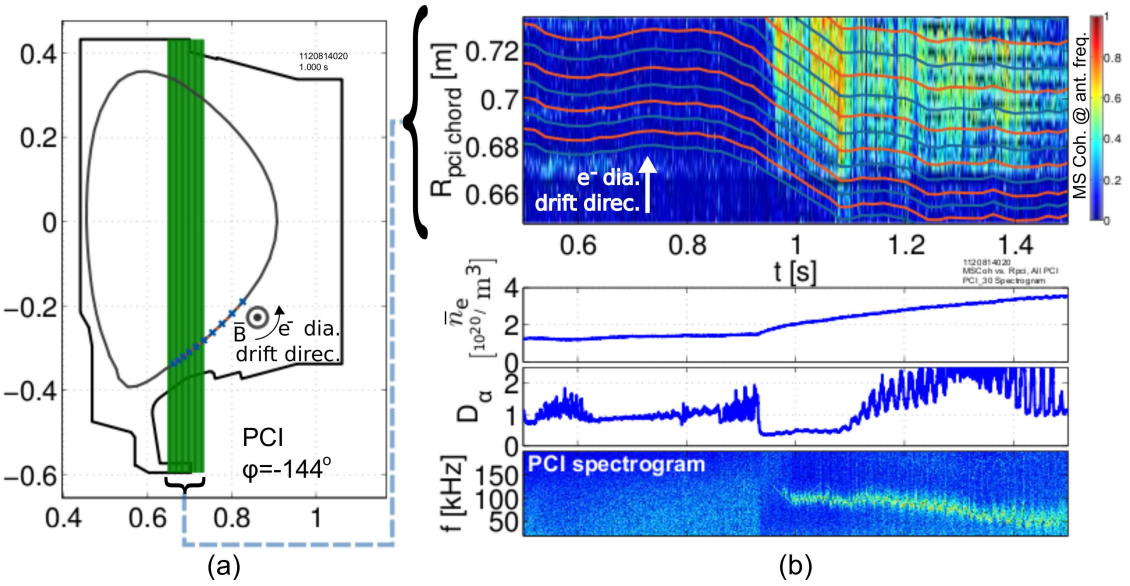

FIG. 11: (a) Poloidal cross section containing PCI chords, as well as mapped locations of antenna rungs. While the PCI chords intersect the LCFS at two points, only the intersection below the midplane maps to the antenna. (b) The magnitude squared coherence at the antenna frequency is plotted in the color axis against major radius and time. This produces a one-dimensional image across the major radial direction of the magnitude squared coherence, which evolves as the discharge progresses. Overplotted in blue and orange lines are the antenna rung locations mapped on the LCFS to the plane containing the PCI chords. The subplots are $\bar{n}_e$ and D_α traces and a spectrogram from a single PCI chord.

Figure 11 provides a stronger indication of field-line guidance. The cross-section containing the PCI chords is shown, again with an illustration of the LCFS and the mapped Shoelace rung locations. In Figure 11b, a time-evolving, one-dimensional image of the induced perturbation is produced by stacking top-to-bottom the magnitude squared coherence at the antenna frequency for each PCI chord, and assembling all such images from each time slice, left-to-right. Overlaid on these images are the evolving locations of the Shoelace rungs mapped to the PCI cross section. The coherent signal is bounded in major radius by the extent reached by the Shoelace antenna rungs. Indeed, the four rungs that map to the smallest major radii mostly do not overlay with a perturbation, perhaps because of the increased gap between the plasma and the rungs at the lower portion of the antenna. Moreover, in the later part of the discharge, PCI seems to resolve very narrow lines of perturbation tracking

closely the mapped rung locations. It should be noted that the electron diamagnetic drift direction points toward the outward major radial direction (toward the top of the plot, as shown in the figure) at the location on the LCFS where the antenna maps to the PCI chords. One might conjecture that the lack of a driven fluctuation below the lowest rungs of the antenna in Figure 11 might be because the driven perturbation cannot propagate into this region. However, in reverse-field discharges, for which the electron diamagnetic drift velocity points in the opposite direction, the driven response is still restricted to mapped field lines, and the inner-most chords still do not observe a coherent response.

In fact, the field-line mapping criterion predicts accurately which diagnostics do and do not observe the driven perturbation. Figures 6 and 7 show top-down (R,ϕ) and unwrapped side-on (ϕ, z) views of the mapped field lines, together with the locations of a number of fluctuation diagnostics. Only the fluctuation diagnostics which map to the Shoelace antenna - namely, the PCI chords, one to three polarimeter chords, and a subset of Mirnov coils - ever observe a signal coherent with the antenna current.

It is interesting that the driven perturbation is localized to field lines mapping to the antenna, while the QCM is global on the low-field side, especially since we might expect the driven perturbation to drift across field lines. A response strongly guided by magnetic field lines is reminiscent of resonance cones[51–56] describing, for example, the propagation of electrostatic, cold plasma modes, and in particular, the low-frequency electrostatic ion wave branch. Recall also that a field-guided response was observed by Borg *et al.* in experiments on the `TORTUS` tokamak using a single dipole antenna, corresponding to a single field-aligned rung on the Shoelace antenna, driven below the ion cyclotron frequency and intended to excite shear Alfvén waves[34], whose group velocity also runs parallel to the magnetic field. However, the electron-ion collision time in the plasma edge for these discharges is $\tau_{ei} \approx 100$ ns, such that $\tau_{ei}^{-1}/\omega \approx 20$, suggesting strong damping for both the shear Alfvén and electrostatic waves, while the electron-ion collisions are destabilizing for drift waves (compare, e.g., the warm plasma numerical examples in Scott[24] for kinetic shear Alfvén waves, Chap. 4, Sec. VI, and drift waves, Chap. 5, Sec. VIII)[57]. Other properties of the driven mode, discussed below, are also inconsistent with the shear Alfvén and electrostatic wave scenarios. As such, at present, the proper interpretation of the driven mode's guided behavior is still a mystery.

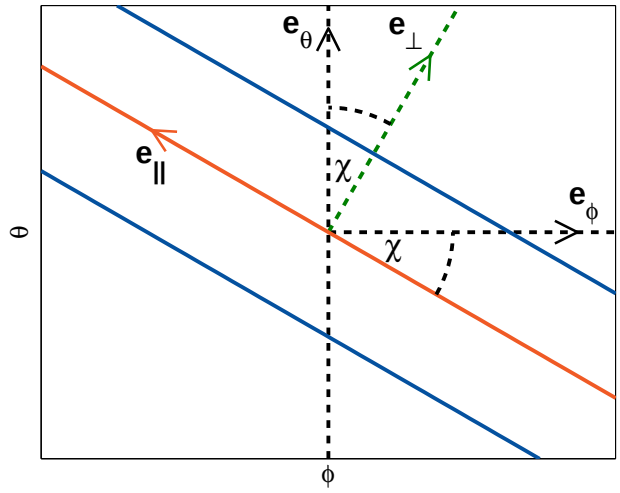

FIG. 12: Schematic of field-aligned coordinate system when viewing inward toward the plasma core. Solid lines correspond to field lines. The directions of the unit vectors are indicated by arrows.

C. Driven Mode Wave Number and Propagation Direction

Thus far, the analysis has focused on the magnitude of the driven fluctuation. By examining its phase across several diagnostics, we may extract mode and wave numbers. Doing so shows that the driven mode has $k_\perp = 1.5$ cm^{-1} at the midplane, precisely the same value as imposed by the antenna winding structure; is approximately field-aligned; and has a phase velocity pointing in the same direction as the electron diamagnetic drift velocity, $\mathbf{v}_* = \nabla p_e \times \mathbf{B}/(n_e e B^2)$.

The PCI diagnostic provides a measurement of the major radial wave number k_R, of the line-integrated density fluctuations. To derive wave numbers resolved within a flux surface, it is necessary to make an assumption about how the mode is localized. It is usually assumed[8,49] that the mode exists in a narrow layer around a single flux surface, and that the PCI measurement, itself, can be localized to the point(s) where the chord intersects the mode's flux surface. Typically, the chords pass through a flux surface at an upper and lower point; however, only the lower intersection maps to the antenna on a field line, and so this ambiguity is removed. In the following, we first take the driven mode to lie nominally on the LCFS, and later explore what happens when this assumed mode layer is varied across other, nearby flux surfaces.

To aid in the calculation of wave numbers, we employ the ballooning coordinate system

described by Dudson *et al.*[58]. The coordinate, z, associated with a test point corresponds to the toroidal angle, ϕ, of the location at the outer midplane, $\theta = 0$, which maps on a field line to the test point. y is the poloidal angle, θ, of the test point; when z is held constant, varying y results in advancing along a field line. Here, the test points correspond to the intersections between the PCI chords and the mode surface.

Figure 12 motivates a procedure for extracting a perpendicular wave number. The parallel direction corresponds to y, and the perpendicular direction to z. We relate the phase angle of the fluctuation signals, α, to the y and z coordinates associated with the PCI chords through the expression, $-\alpha_\ell = nz_\ell + my_\ell + \alpha_0$, for each chord, ℓ. The negative sign in front of α appears because α is derived from the phaser representation, $y(t) = \Re\left\{|A|\, e^{j(\omega t+\alpha)}\right\}$, while the mode number corresponds to the traveling wave, $e^{i(n\phi-\omega t)} = e^{j(\omega t-n\phi)}$ (taking $j = -i$). $n = -\frac{\partial \alpha}{\partial z}$ is just the toroidal mode number. The corresponding wave number is $k_\phi = n/R$. Approximating the mode as field-aligned, $\mathbf{k} = k_\perp \hat{\mathbf{e}}_\perp$, and $-\alpha_\ell = nz_\ell + \alpha_0$. To obtain $k_\perp$ given n, we take k_ϕ to be the projection of $\mathbf{k}$ onto the $\hat{\mathbf{e}}_\phi$ direction holding $y = \theta$ constant, such that

$$k_\perp = \frac{n}{\sin(\chi)\, R} \tag{1}$$

where $\tan(\chi) \equiv \frac{\sqrt{B^2 - B_\phi^2}}{B_\phi} = 1/\nu$, with $B_\phi = \mathbf{B} \cdot \hat{\mathbf{e}}_\phi$ the toroidal field strength, $\nu \equiv \frac{\mathbf{B}\cdot\nabla\phi}{\mathbf{B}\cdot\nabla\theta}$ the local field-line pitch[58], and χ and R are evaluated at the outer midplane.

The quality of the fit under the field-aligned approximation is apparent from Figure 13, which plots the phase angle, α, of each chord against the z coordinate, together with the least-squares fit to $-\alpha_\ell = nz_\ell + \alpha_0$ from the outer 21 chords[59], using spectral analysis over a ~ 3 ms time slice. Note that α is "unwrapped" - differences between the phases of adjacent chords greater than or equal to π are eliminated by adding multiples of $\pm 2\pi$. The field-aligned approximation captures the phase progression across the PCI chords extremely well. As such, it may be concluded that taking $k_\perp \gg k_\parallel$ introduces a negligible error in the estimate for $k_\perp$.

On the other hand, it is difficult to measure $k_\parallel$ using the PCI diagnostic. This is because the intersections between the chords and the lower LCFS span a poloidal range of $\theta_{32} - \theta_1 \approx 15^\circ$. By contrast, the range of z spans $\gtrsim 60^\circ$. These ranges, combined with the expectation (derived from the QCM) that $k_\perp \gg k_\parallel$, means that the PCI diagnostic cannot provide a good measurement for $k_\parallel$, since most of the phase difference across the chords is due to the

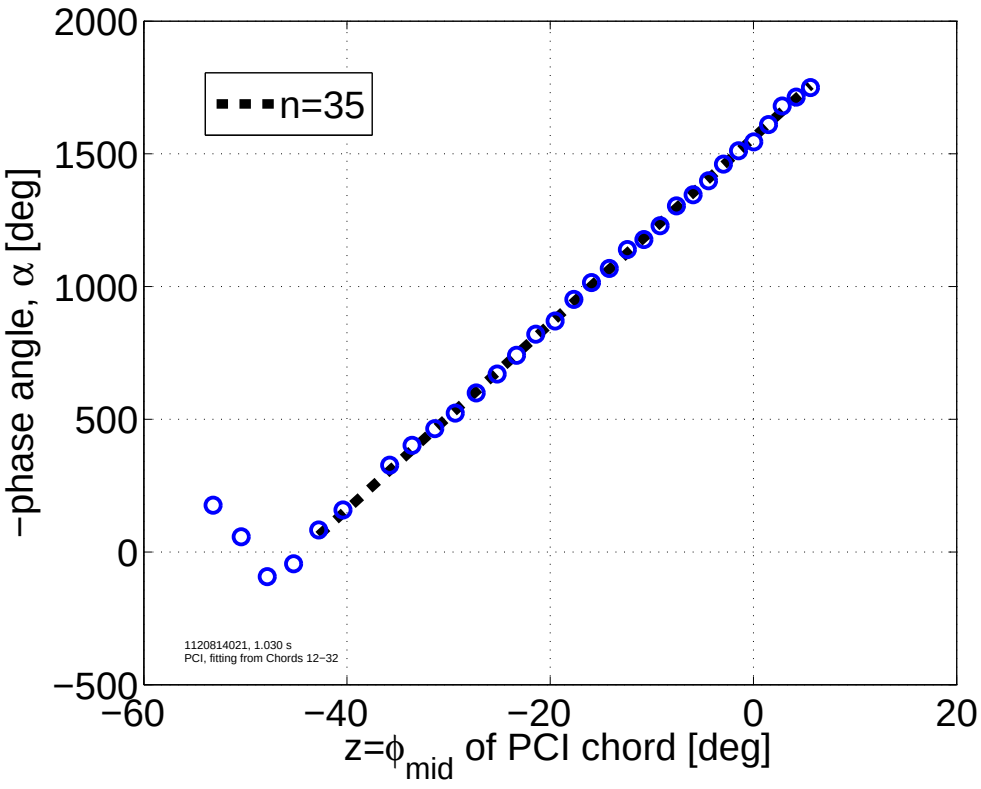

FIG. 13: Quality of fit of expression, $-\alpha_\ell = nz_\ell + \alpha_0$ across all PCI chords, ℓ. z_ℓ is the toroidal angle at the outer midplane (ϕ_{mid}) of the point which maps on a field line to the lower intersection of PCI chord, ℓ, with the LCFS.

phase progression in the perpendicular direction.

Figure 14 (Multimedia view) shows the result of performing the calculation for $k_\perp$ using PCI data. Prior to the onset of H-mode, there is no coherent signal in the density fluctuation, and so the calculated value for $k_\perp$ varies randomly and rapidly. However, immediately after the H-mode transition, $k_\perp$ of the coherent signal locks to the value imposed by the antenna winding structure, namely, 1.5 cm^{-1}. Moreover, the sign corresponds to propagation in the laboratory frame in the same direction as the electron diamagnetic drift velocity.

Figure 14b (Multimedia view) reports data from a reverse-field discharge which had an early ELM-free H-mode (not EDA H-mode, and without an apparent QCM), followed by a back-transition to Ohmic L-mode, and finally terminating in a disruption. For reference, a spectrogram from this discharge of a single PCI chord is reproduced in Figure 16, accompanied by density and D_α traces. Here, again, during H-mode, $k_\perp$ settles precisely on the magnitude imposed by the antenna winding. However, now, the sign is negative, following

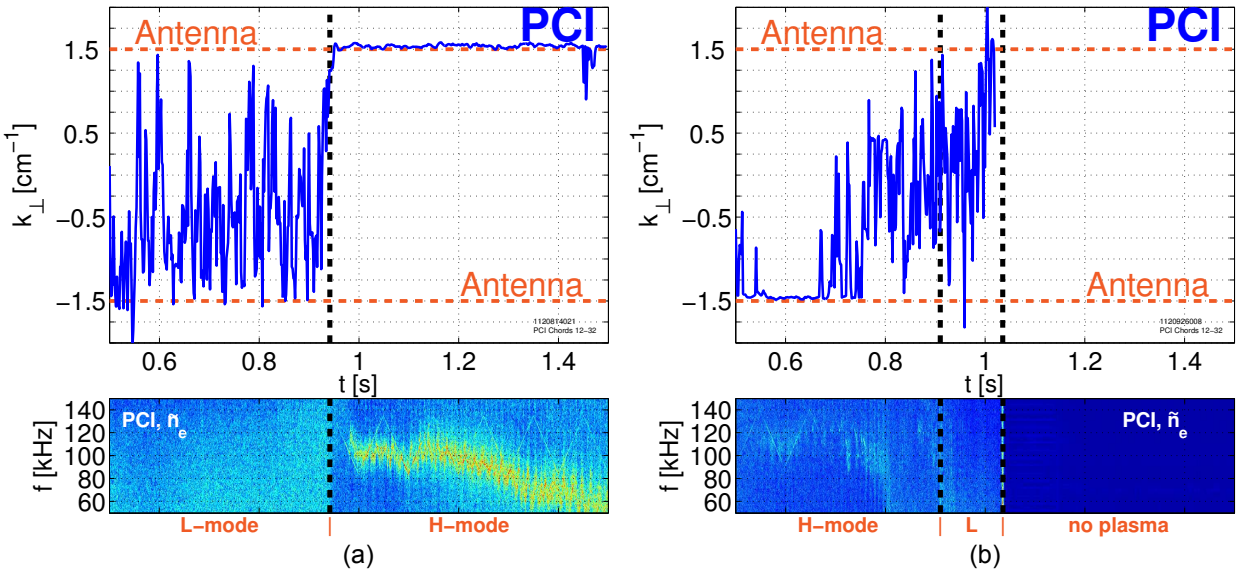

FIG. 14: (a) Calculation of $k_\perp$ using the phase progression of the cross-power between the antenna current and the PCI chords from each time slice of the coherence spectrogram; a spectrogram from a PCI chord appears underneath, showing both the QCM and the Shoelace-driven perturbation. The sign of $k_\perp$ indicates propagation in the same direction as the electron diamagnetic drift velocity. (b) In this reversed field discharge, the value $k_\perp$ for the driven fluctuation changes sign, consistent with the inversion of the electron diamagnetic drift direction. H-mode is lost just after 0.8 s, after which time the antenna produces no coherent density response. See supplemental material at (a) [URL will be inserted by AIP] and (b) [URL will be inserted by AIP] for animations showing the time-evolving ω vs. k_R diagram from the cross-power between PCI and the antenna current, together with subplots showing the time-evolving magnitude squared coherence and the final calculation of $k_\perp$. The antenna perturbation appears as a feature with fixed k_R and scanning frequency. (Multimedia view)

the reversal of the field and electron diamagnetic drift directions.

It is prudent to examine how the assumption that the driven mode is localized to the LCFS affects the estimate for $k_\perp$. Figure 15a shows the result of repeating the $k_\perp$ calculation after assuming the mode is localized on each of 21 uniformly-spaced flux surfaces between $0.95 \leq \bar{\psi} = (\psi - \psi_0)/(\psi_{LCFS} - \psi_0) \leq 1.05$; at the midplane, this corresponds to a range from ~ 8 mm inside to ~ 8 mm outside the LCFS. The field-aligned approximation is still employed. The inset shows the value of $k_\perp$ obtained for each flux surface for a particular

$\sim$ 3 ms time slice around 1.20 s. The dashed lines highlight the FWHM band, $k_\perp = 1.5 \pm 0.1$ cm^{-1}, expected for the antenna's winding structure. The estimate for $k_\perp$ is robust against uncertainty in the identity of the flux surface to which the mode is localized. This is because the field lines that map the PCI chords to the midplane over this range of flux surfaces do not pass close enough to the x-point to experience significant magnetic shear. In fact, we might attempt to use this procedure to localize the driven fluctuation based on $k_\perp$-matching considerations; doing so would suggest that the driven mode sits in a layer between $0.98 \lesssim \bar{\psi} \lesssim 1.048$ ($-3 \lesssim R_{mid} - R_{mid,LCFS} \lesssim 7.5$ mm). However, this estimate is subject to error from the EFIT reconstruction. Nonetheless, it is consistent with the expectation that the mode is localized in the edge, near the LCFS and overlapping with the QCM layer.

The phase information may also be reported directly as the toroidal mode number, n. This is done in Figure 15b. Here, the toroidal mode number obtained from the outer 21 chords of the PCI diagnostic is compared with that from two Mirnov coils spaced 4.8 toroidal degrees apart. Note that the field-aligned approximation is not applied to the analysis of the Mirnov coils, since they are displaced only in the toroidal angle. The values obtained from the two diagnostics are comparable, though there is a discrepancy between the stable value from PCI (between 31 and 34) and the Mirnov-supplied value prior to H-mode (during which time there is no coherent $\tilde{n}_e$), and in the later part of the discharge. The lines labeled "antenna" correspond to the toroidal mode number for a field-aligned perturbation with $k_\perp = 1.5$ cm^{-1}; the positive line closely matches the measured toroidal mode number. Because the antenna drives a coherent $\tilde{B}_\theta$ response for the entire discharge, the Mirnov coils provide a measurement of n for the induced fluctuations prior to the onset of H-mode.

The fact that the toroidal mode numbers calculated from PCI (giving measurements of the driven mode below the midplane, and determined assuming $k_\parallel = 0$) and Mirnov coils (placed at a different poloidal angle above the midplane, and calculated without any assumption about $k_\parallel$) gives further confidence in approximating the driven mode as field-aligned, $k_\perp \gg k_\parallel$. This is consistent with a drift wave response, which tends to select the longest parallel wavelength. This wavelength is often estimated to be twice the connection length, $L_c \approx 9$ m$\sim q_{95}\pi R$, which connects a point near the lower (upper) x-point to the top (bottom) of the plasma on a field line spanning the bad curvature region; doing so yields $k_\parallel \sim \pi/L_c = 0.0035$ cm$^{-1} \ll k_\perp = 1.5$ cm^{-1}.

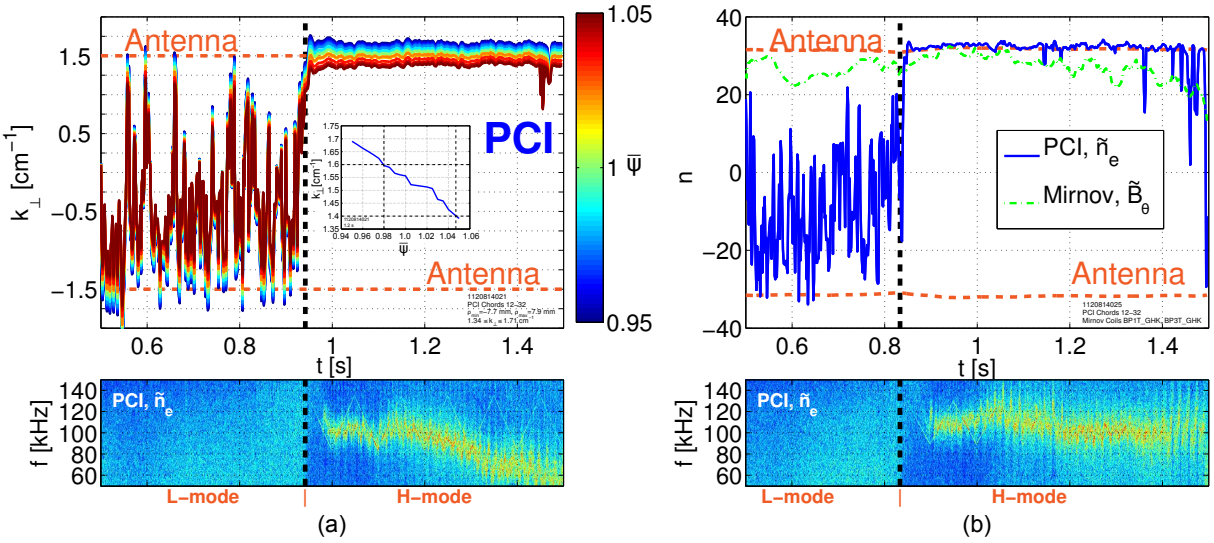

FIG. 15: (a) Calculation of $k_\perp$ under field-aligned approximation, but taking the driven mode to be localized on any of 21 uniformly-spaced flux surfaces between $0.95 \leq \bar{\psi} = (\psi - \psi_0)/(\psi_{LCFS} - \psi_0) \leq 1.05$, as depicted by the line color; at the midplane, this corresponds to a range from ~ 8 mm inside to ~ 8 mm outside the LCFS. Inset: the value of $k_\perp$ obtained for each flux surface during a ~ 3 ms time slice around 1.20 s. The dashed lines highlight the FWHM band, $k_\perp = 1.5 \pm 0.1$ cm^{-1}, expected for the antenna's winding structure. (b) Toroidal mode number derived from Mirnov coils, as well as PCI measurements, from a different discharge. The Mirnov coils pick up a coherent response in $\tilde{B}_\theta$ for the entire antenna pulse, allowing a measurement of n for the driven fluctuations prior to the onset of H-mode. Also included is the antenna toroidal mode number corresponding to $k_\perp = \pm 1.5$ cm^{-1} for a field-aligned perturbation. The subplot shows a spectrogram from a single PCI chord.

The role of $\mathbf{E} \times \mathbf{B}$ flow also needs to be considered. Recent measurements with the MLP[11] for ohmic EDA H-mode discharges like the ones discussed here have shown that in the QCM mode layer, the radial electric field points outward, such that the $\mathbf{E} \times \mathbf{B}$ and electron diamagnetic flows oppose one another. As such, the QCM propagates in the electron diamagnetic drift direction in both the laboratory and plasma frames. But ~ 1 mm inward from the LCFS, the $\mathbf{E} \times \mathbf{B}$ flow changes directions, with $\mathbf{v_E} = \mathbf{v}_*$ at ~ 2 mm inside the LCFS. If the antenna-driven mode overlaps spatially with the QCM, as assumed above, then it also rotates in the electron diamagnetic drift direction in both the plasma as well as the

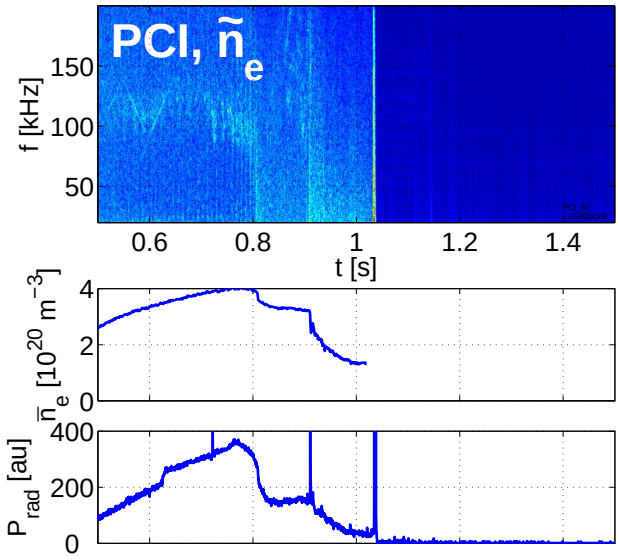

FIG. 16: Spectrogram of reversed-field discharge in which a resonant response to the antenna appears on the diagnostic signals, but where there is no apparent intrinsic QCM.

laboratory frame. However, a precise measurement of the driven mode layer is necessary in order to make this statement with certainty.

D. Transfer Function Analysis

Up until now, we have focused on the coherence of fluctuations in short (∼3 ms) time slices. It is also instructive to examine the response across an entire frequency scan, typically covering ∼40 kHz, by examining the transfer function, an analysis technique commonly employed in the Active MHD literature[36,40,43,44]. The transfer function, $H(j\omega)$, can be thought of as the coherent output registered in the signal, y (e.g. output from a PCI chord or a Mirnov coil), caused by, and related linearly to, the input signal, x (here, the antenna current). It is calculated from $H(j\omega) = P_{xy}/P_{xx}$, where again, P_{xy} is the complex cross power spectral density between signals, x and y, and P_{xx} the power spectral density of x. The transfer function is especially useful in detecting resonances, since it reveals peaks in the coherent response. These peaks can then be characterized by their center frequency (corresponding to the natural resonant frequency of the mode), bandwidth (corresponding to the damping rate), and overall magnitude.

Indeed, the frequency response of the Shoelace antenna is strongly peaked in H-mode,

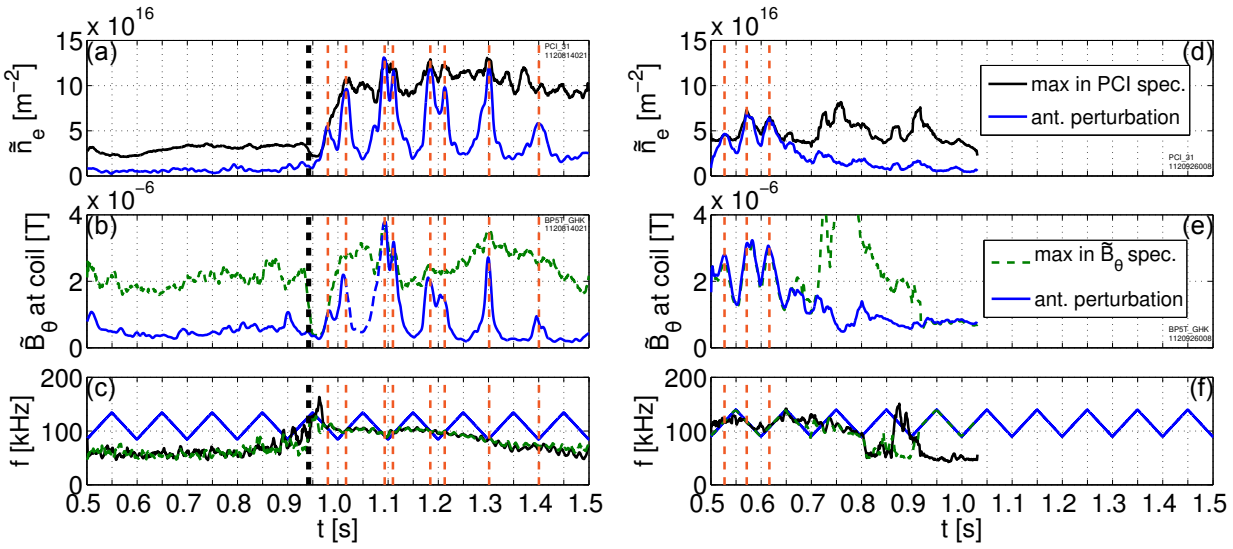

FIG. 17: Magnitude of coherent response, $x|P_{xy}/P_{xx}|$, where x is the antenna current and y is the fluctuation signal, for (a,b,c) a forward-field shot with an intrinsic QCM and (d,e,f) a reverse-field shot with no prominent intrinsic QCM. The responses are from (a,d) a PCI chord and (b,e) a Mirnov coil. The bottom subplots (c,f) show the antenna drive frequency (blue solid line), together with the peak frequencies in the PCI (black solid) and Mirnov coil (green dashed) spectra. Orange vertical dashed lines highlight peaks in the coherent response.

but not in L-mode. Figure 17 illustrates this point. It shows an estimate for the absolute amplitude of the coherent response obtained by scaling the transfer function by the antenna current amplitude, $|H \cdot I_a|$. Both the line integrated density fluctuation, $\tilde{\bar{n}}_e$, from a PCI chord and the poloidal field fluctuation, $\tilde{B}_\theta$, measured at a Mirnov coil are shown[60]. For comparison, the amplitude of the maximum spectral component of the fluctuation signal in the band from 40 to 200 kHz is overplotted. The frequency of the maximum component for each fluctuation signal is included in a subplot, together with the antenna frequency. The data on the left-hand side (Figure 17a-c) are from the same discharge as that shown in Figure 9, which had a fully-developed EDA H-mode with a QCM. The data on the right-hand side (Figure 17d-f) correspond to the discharge in Figure 16, which had a short-lived ELM-free H-mode and no prominent QCM.

When the antenna frequency crosses the peak in the PCI spectrum - a proxy for the QCM center frequency - we see a sharp peak in the coherent response, such that the amplitude of

the coherent fluctuation matches the peak amplitude in the spectrum. This is true for both $\tilde{\tilde{n}}_e$ and $\tilde{B}_\theta$ measurements. We may wonder whether the antenna is driving a fluctuation of this amplitude, or is locking the intrinsic mode to its own phase. The second possibility might seem more plausible given that the total peak fluctuation amplitude increases only slightly when the antenna crosses the QCM frequency.

However, in experiments examining nonlinear interaction between a driven mode and a coherent drift wave structure on a linear device, Brandt *et al.*[33] observed frequency pulling and the appearance of sidebands in the fluctuation spectra. These features are not apparent in the fluctuation spectra obtained during Shoelace antenna operation, though higher antenna power may be needed to access this behavior.

In addition, in the case where there is no apparent QCM, the response is still peaked around a particular frequency, as shown in the data in Figure 17d-f, suggesting a resonance. During the ELM-free H-mode, the coherent response dominates the PCI spectrum most of the time, and the Mirnov coil response all of the time. The peaks in the density response are shallower than, but still comparable to, those in the EDA case in 17a-c. This is a significant result, and suggests that, on mapped field lines, the antenna might be able to drive a fluctuation close to the level of an intrinsic QCM, even when no such intrinsic mode is present. Given the QCM's role in regulating the pedestal, we might also speculate that the antenna drives transport on mapped field lines similar to the intrinsic mode; further experiments are necessary to investigate this exciting possibility.

Before proceeding, it is important to point out that when the field pitch angle evolves during the discharge, it is necessary to remove a phase offset. This was not necessary in the calculation of mode numbers using the short-time spectral analysis because the time slices were on the order of $\sim$3 ms, and the pitch angle evolves on a longer time scale, as evidenced by the mapped rung locations overplotted on the time-evolving 1D coherence image in Figure 11. However, over the course of a complete frequency scan, lasting 50 ms in these experiments, the pitch angle can change appreciably. This effect may be accounted for in the transfer function as $H(j\omega) = H_c(j\omega)e^{-jn\Delta z}$, where the subscript, c, denotes calibration, and Δz the change in the toroidal angle after mapping to the outer midplane.

Figure 18 shows the transfer function magnitude and phase over a single frequency scan from three mapped diagnostics: a PCI chord, a Mirnov coil, and a polarimeter chord. The data are from the same forward-field discharge described in Figure 17a-c. The magnitudes

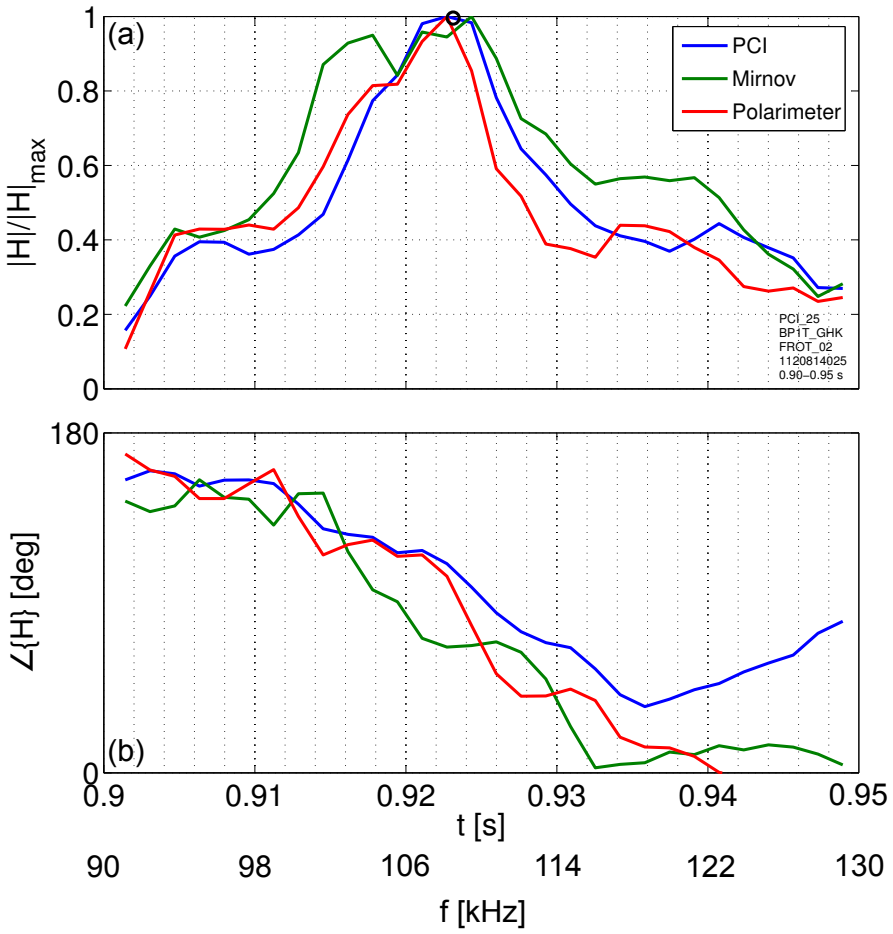

FIG. 18: (a) Transfer function magnitude for a PCI chord, a Mirnov coil, and a polarimeter chord over a single frequency scan, normalized to the maximum value over the scan for each diagnostic to allow comparison. (b) Phase of the transfer function over the course of the same scan, adjusted by the phase offset, $n\Delta z$, to account for the change in the mapped toroidal angle, Δz, for each diagnostic, following the mapping procedure described in Section IV C.

are normalized by the maximum value over the scan so that data from different diagnostics can be compared, while the phase is adjusted according to the discussion above. The peak frequency, FWHM, and relative phase transition match across the three diagnostics. The relative change in phase of 180° over the frequency scan further suggests that the response may be modeled as a simple pole using an expansion of the form,

$$H_c(j\omega) = H_0 + \frac{A}{\gamma + j(\omega - \omega_0)} + \frac{A^*}{\gamma + j(\omega + \omega_0)} \tag{2}$$

where H_0 is a real constant offset, A is the complex residue, A^* its complex conjugate, γ the

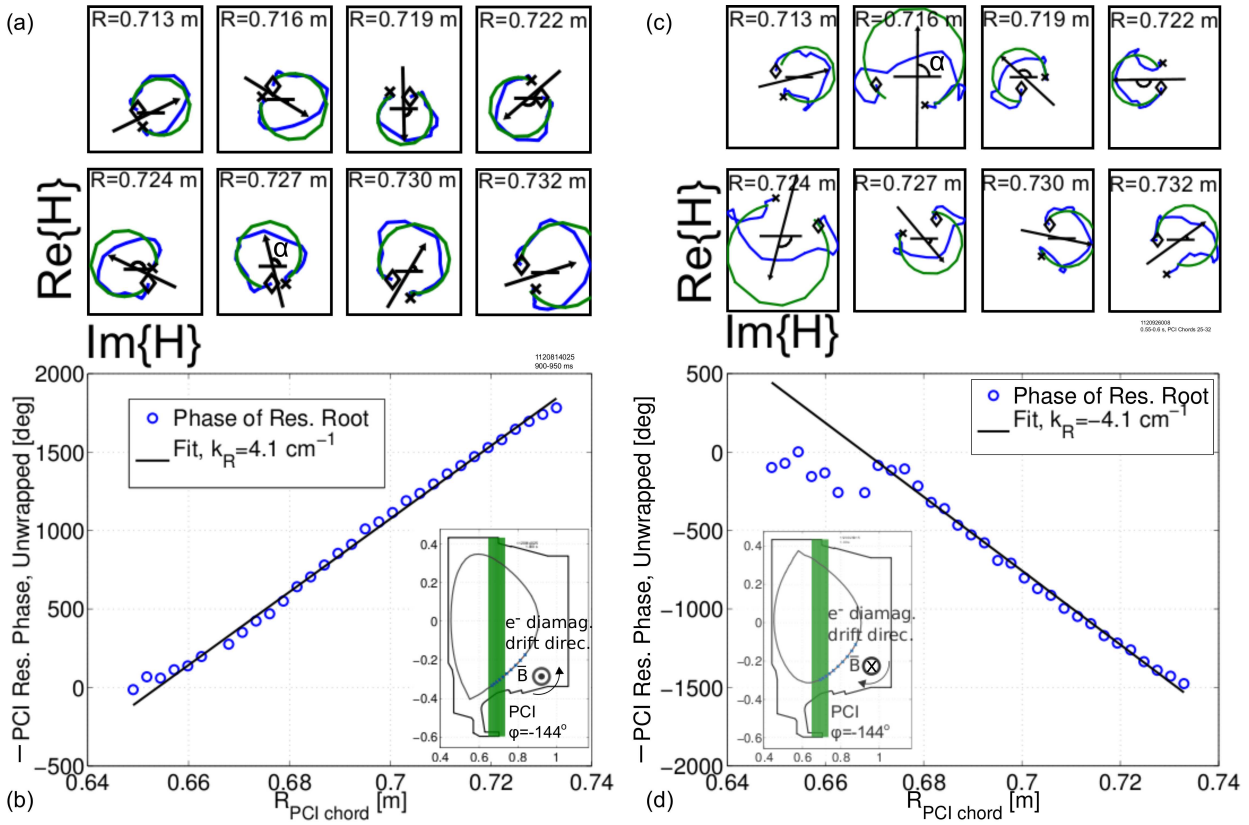

FIG. 19: (a) Plot in complex plane of transfer function, H, for eight outer-most PCI chords (blue solid line), together with parameterized fit using Eq. 2 (green solid line). Arrows indicate phase angle of residue, A. The fact that circular trajectories of H are advancing in the clockwise direction for increasing frequency is indicative of a damped resonance. (b) Plot of -1 multiplied by the unwrapped phase angle of each pole residue from each chord versus corresponding chord major radius. The slope gives the major radial wave number, k_R. An inset shows Shoelace mapping on the LCFS in the PCI plane, as well as the B_ϕ and electron diamagnetic drift directions. (c,d) Here, the data is from a discharge with reversed field. Again, the sign of k_R is flipped, following the inversion of the electron diamagnetic drift direction. No QCM was present in this discharge, but the antenna response still appears to be a weakly-damped resonance.

damping rate, ω_0 the resonant angular frequency, and the property that $H(-j\omega) = H^*(j\omega)$ ensures a purely real output signal. The residue, damping rate, and resonant frequency may then be used to characterize the peak.

Figure 19 examines the transfer function for a forward-field shot with a strong QCM (Figure 19a,b), as well as a reversed-field shot with no apparent QCM (Figure 19c,d). In

both cases, the plot of the transfer function in the complex plane (the Nyquist plot), shown with a blue solid line, executes a circular trajectory, rotating in the clockwise direction for increasing frequency. The green solid line plots Eq. 2 with parameters fit to the same peak; this functional form always appears as a circle in the complex plane, circulating in the clockwise direction when $\gamma > 0$ (implying a damped response).

The phases, α, of the pole residues, A, used to fit the transfer function are also tracked and unwrapped, again revealing a major radial wave number, k_R, that (a) matches the antenna $k_\perp$ after assuming a field-aligned structure and mapping to the midplane, and (b) points in the direction of the electron diamagnetic drift direction, flipping sign between the forward- and reverse-field cases.

Having closely analyzed the phase of the residue, we may investigate the other fit parameters of Eq. 2. Figure 20a plots the resonant frequency, $f_0 = \omega_0/(2\pi)$, for each frequency scan, along with the peak in the PCI spectrum (black solid line) and the antenna drive frequency (black dashed line). f_0 is reproduced with little scatter across multiple PCI chords (blue solid lines), Mirnov coils (green solid lines), and polarimeter chords (red solid lines). Moreover, it tracks very closely the frequencies at which the antenna drive crosses the peak PCI frequency, recovering the result mentioned earlier that the peak frequency matches the QCM frequency when there is a QCM present. It is also interesting that, when the antenna frequency approaches the peak in the PCI spectrum, the peak tends to follow the drive briefly.

Figure 20b shows the damping rate, γ, normalized by 2π for comparison with the resonant frequency. The error bars correspond to the standard deviation across independent measurements of an individual diagnostic. A damping rate of $\gamma/\omega \approx\sim 5\%$ appears across all diagnostics. The damping rate in the reversed field discharge shown in Figure 17d-f is higher - around 10% - and displays more scatter across the diagnostics. The range, $\gamma/\omega_0 = 0.05 - 0.1$, is typical of these experiments, indicating that the driven mode is only weakly damped.

V. CONCLUSIONS AND FUTURE WORK

A new "Shoelace" antenna was used for the first time to drive fluctuations in the Alcator C-Mod tokamak edge. The field-aligned antenna winding imposes a particular $k_\perp = \pm 1.5 \pm$

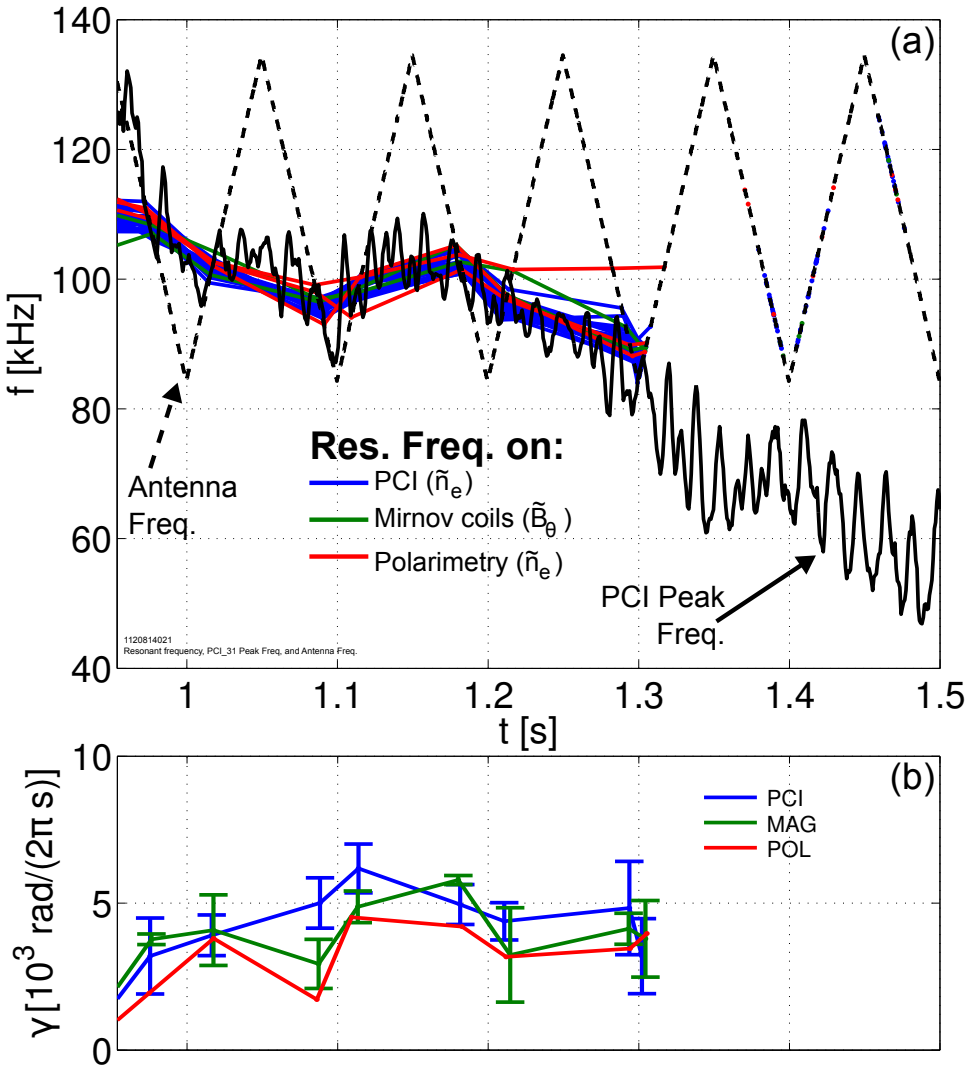

FIG. 20: (a) Resonant frequency from PCI (blue solid lines), Mirnov coils (green solid), polarimetry (red solid); antenna freq. (black dashed); peak PCI freq. (black solid). The resonant frequency tends to track the QCM frequency, whose proxy here is the peak in the PCI spectrum. (b) Damping rate across discharge, as determined by transfer function between antenna current and fluctuation signals from a Mirnov coil, a PCI chord, and a polarimeter chord. Damping rates from a wide variety of discharges are low, settling to a value between $\gamma/\omega_0 = 5 - 10\%$, where ω_0 is the resonant angular frequency.

0.1 cm^{-1}, with toroidal mode number, $n = \pm 35 \pm 23$, while a custom-built wide-band matching network allows operation in a broad frequency range from 45-300 kHz. These wave number and frequency ranges were chosen primarily to cover the parameters normally

observed for the QCM, which regulates the pedestal in the ELM-free, steady-state EDA H-mode regime. However, they also cover part of the parameter range of the WCM, which accompanies the I-mode regime. 2 kW of RF power are provided by two commercial 50 Ω amplifiers.

The antenna was energized during a number of ohmic L- and H-mode plasmas. In H-mode plasmas, the antenna drove density and magnetic field perturbations in the edge, while in L-mode plasmas, only magnetic field perturbations were induced. The driven mode always propagated in the electron diamagnetic drift direction in both forward- and reverse-field operation, and was approximately field-aligned, with $k_\perp$ and n matching the values imposed by the antenna winding. The driven fluctuations were also guided by field lines.

Moreover, the driven response was strongly peaked around a specific frequency in H-mode, but not in L-mode. In EDA H-mode discharges with an intrinsic QCM, the resonance fell precisely on the QCM center frequency. However, even in ELM-free H-mode discharges without a prominent QCM, the antenna response was still peaked. In both cases, the damping rate was weak, with $\gamma/\omega_0 \approx 5-10\%$, with the lower end of the range corresponding to EDA H-mode discharges. At the resonant frequency, a large fraction of the total $\tilde{n}_e$ and $\tilde{B}_\theta$ fluctuation was strongly coherent with the antenna current. In discharges with a QCM, it is possible that the antenna locked the intrinsic mode phase to its own. In discharges without a strong QCM, the antenna-induced fluctuation seemed to dominate the QCM range of the $\tilde{n}_e$ and $\tilde{B}_\theta$ spectra. This is significant in that it suggests the driven mode may be driving transport in a similar fashion to, but in the absence of, the intrinsic QCM.

The antenna-driven mode shares the same $k_\perp$, frequency, and propagation direction as the QCM, with $k_\perp \gg k_\parallel$, is localized to the edge, only exhibits a density fluctuation after the development of steep edge gradients in H-mode, and is guided by field lines. The guided behavior is reminiscent of resonance cones predicted for low-frequency electrostatic waves[51–55], as well as shear Alfvén waves[34], but these scenarios are not consistent with the high collisionality ($\tau_{ei}^{-1}/\omega \approx 20 \gg 1$) of the edge, nor the driven resonance around the QCM.

Experiments in linear devices have shown that exciting mode-selective parallel currents is the essential ingredient for coupling to drift waves, and that this may be done inductively[33]. As such, it is tempting to identify the driven mode with the QCM, which has been identified as an electron drift wave with additional interchange and electromagnetic character[11]. However, at present, we do not have the same detailed diagnostic information[61] of the driven

mode as is available for the intrinsic QCM, and so it is difficult to conclusively verify this association.

Examining the driven mode using the Mirror Langmuir Probe (MLP) would allow us to (a) identify the degree of spatial overlap between the intrinsic QC and driven modes, (b) determine the phase difference between the different fluctuation quantities (especially electron pressure, $\tilde{p}_e$, and potential, $\tilde{\Phi}$) to characterize the driven mode physics, (c) examine via local measurements whether the antenna affects the amplitude, phase, or stability of the intrinsic mode, (d) determine whether the antenna imparts torque to the plasma, and (e) crucially, learn whether the antenna-induced mode independently drives transport. Such an investigation was not possible in the initial round of experiments because the antenna was not field-aligned for pitch angles at which the antenna mapped to the MLP location. The antenna has since been prepared for the next experimental campaign by rewinding at a new angle which does map to the MLP.

The Shoelace antenna power system is capable of locking in real-time to an analog signal with a coherent feature in the QCM band, 50-150 kHz, from a fluctuation diagnostic, adding a phase delay tunable in 64 steps between 0 and 360 degrees. The construction of this system will be described elsewhere[48]. The operation of the system was demonstrated in initial experiments, as shown in Figure 21. Here, a spectrogram of a PCI signal is accompanied by traces of the PCI peak (blue solid line) and antenna drive (green solid line) frequencies, as well as the antenna current. The antenna frequency closely tracks the rapidly-varying PCI peak frequency, while the antenna current remains near 80 A throughout the discharge as the matching network continually adjusts its tuning following the changing frequency. Feed-forward amplitude modulation was applied to the current program to help distinguish the antenna-driven fluctuation from the intrinsic QCM.

The phase lock system was built to explore whether the antenna may feedback stabilize, or further destabilize, the intrinsic QCM, and whether it may also impart a torque to the plasma, in an analogous manner to an AC motor, where the antenna plays the role of the stator and the current filaments of the QCM, the rotor. However, only preliminary work was carried out with this system, and further experiments are needed to determine whether or not the antenna may be used in this way.

Lastly, while 2 kW of input power were available to the Shoelace antenna, the matching network and winding are built to allow expansion to 10 kW. Power scans enabled by an

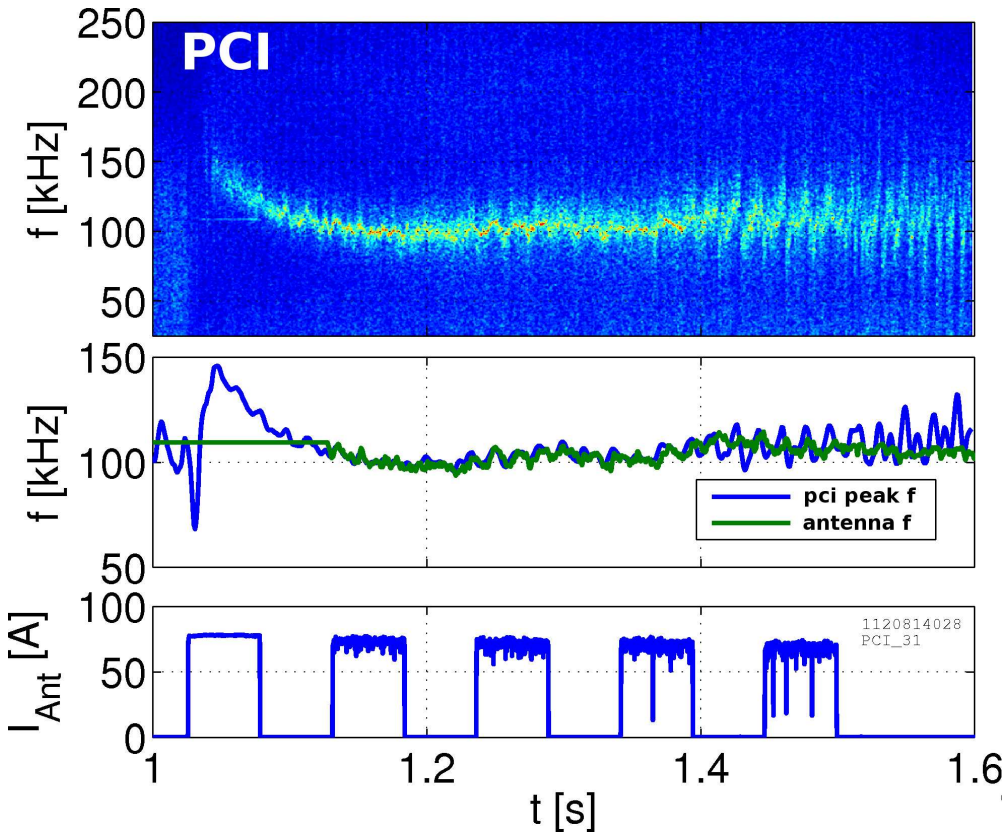

FIG. 21: A real-time frequency lock of the antenna drive to a QCM feature in the PCI signal has already been demonstrated in experiments.

increase in available input could (a) help us understand how fluctuation-driven transport correlates to mode amplitude, (b) learn how much additional power a nonlinearly-saturated QCM can accept, and (c) possibly explore nonlinearities in the antenna response (answering, for example, the question of whether doubling antenna current results in doubling the driven mode amplitude).

Accompanying the experimental effort, we have begun modeling the antenna/plasma interaction using `BOUT++`, a highly-adaptable framework for performing plasma fluid simulations in arbitrary, three-dimensional, curvilinear coordinate systems[58]. Initial work has utilized a three-field (pressure (p_e), vorticity ($\bar{\omega} = \mathbf{b} \cdot \nabla \times \tilde{\mathbf{u}}$), and parallel ion velocity $u_{\|}$) slab model with magnetic and flow shear; however, the model will be expanded to include electromagnetic and curvature effects. The goal is to understand the processes which control the measured damping rate, and in addition to construct a minimal model sufficient to explain the antenna coupling to the plasma. We should point out that, as of the preparation of

this publication, simulation of the QCM using BOUT++ remains an active area of research[62], and the precise behavior measured in experiment has not yet been fully captured in the model.

It is the authors' hope that the insight gained in the theoretical effort will help guide future experimental inquiry using the Shoelace antenna on Alcator C-Mod.

ACKNOWLEDGMENTS

The authors express their sincere gratitude to the skilled members of the Alcator C-Mod scientific, engineering, technical, and administrative staff, especially Samuel Pierson, Bruce Wood, David Bellofatto, Maria Silveira, and Andrew Pfeiffer. The authors gratefully acknowledge the collaboration with the Active MHD group at the Joint European Torus, who provided the two source amplifiers used in this study, as well as the collaboration with the BOUT++ group - especially Xueqiao Xu, Ben Dudson, Maxim Umansky, and Ilon Joseph - for many illuminating discussions on the relevant theory, and sincerely thank Professor Bruno Coppi and Dr. Tianchun Zhou for their helpful input. T. Golfinopoulos wishes to thank Dr.'s Jason Sears, Joseph Snipes, Christian Theiler, Matthew Reinke, Steven Wukitch, and Christophoros Vassiliou, as well as Professor David Staelin, for instructive discussions about Active MHD methodology, the QCM, edge physics, and circuit fabrication. This work was supported by USDoE Coop. Agreement DE-FC02-99ER54512.

REFERENCES

[1]A. E. Hubbard, R. L. Boivin, R. S. Granetz, M. Greenwald, J. W. Hughes, I. H. Hutchinson, J. Irby, B. LaBombard, Y. Lin, E. S. Marmar, A. Mazurenko, D. Mossessian, E. Nelson-Melby, M. Porkolab, J. A. Snipes, J. Terry, S. Wolfe, S. Wukitch, B. A. Carreras, V. Klein, and T. S. Pedersen, Phys. Plasmas (1994-present) **8** (2001).

[2]R. M. McDermott, B. Lipschultz, J. W. Hughes, P. J. Catto, A. E. Hubbard, I. H. Hutchinson, R. S. Granetz, M. Greenwald, B. LaBombard, K. Marr, M. L. Reinke, J. E. Rice, D. Whyte, and A. C.-M. Team, Phys. Plasmas (1994-present) **16**, 056103 (2009).

[3]K. H. Burrell, M. E. Austin, D. P. Brennan, J. C. DeBoo, E. J. Doyle, P. Gohil, C. M. Greenfield, R. J. Groebner, L. L. Lao, T. C. Luce, M. A. Makowski, G. R. McKee, R. A.

Moyer, T. H. Osborne, M. Porkolab, T. L. Rhodes, J. C. Rost, M. J. Schaffer, B. W. Stallard, E. J. Strait, M. R. Wade, G. Wang, J. G. Watkins, W. P. West, and L. Zeng, Plasma Phys. Control. Fusion **44**, A253 (2002).

[4]K. Kamiya, M. Bakhtiari, S. Kasai, H. Kawashima, Y. Kusama, Y. Miura, H. Ogawa, N. Oyama, M. Sato, K. Shinohara, K. Tsuzuki, K. Uehara, and J.-M. Group, Plasma Phys. Control. Fusion **46**, A157 (2004).

[5]E. Belonohy, G. Pokol, K. McCormick, G. Papp, S. Zoletnik, and the W7AS Team, AIP Conf. Proc. **993**, 39 (2008).

[6]Y. Takase, R. Boivin, F. Bombarda, P. Bonoli, C. Fiore, D. Garnier, J. Goetz, S. Golovato, R. Granetz, M. Greenwald, S. Horne, A. Hubbard, I. Hutchinson, J. Irby, B. LaBombard, B. Lipschultz, E. Marmar, M. May, A. Mazurenko, G. McCracken, P. O'Shea, M. Porkolab, J. Reardon, J. Rice, C. Rost, J. Schacter, J. Snipes, P. Stek, J. Terry, R. Watterson, B. Welch, and S. Wolfe, Proceedings, 16th International Conference on Fusion Energy, Montreal 1996 **1**, 475 (1997).

[7]M. Greenwald, R. Boivin, P. Bonoli, C. Fiore, J. Goetz, R. Granetz, A. Hubbard, I. Hutchinson, J. Irby, Y. Lin, E. Marmar, A. Mazurenko, D. Mossessian, J. Sunn Pederson, T. Rice, J. Snipes, G. Schilling, G. Taylor, J. Terry, S. Wolfe, and S. Wukitch, Plasma Phys. Control. Fusion **42**, A263 (2000).

[8]J. Snipes, B. LaBombard, M. Greenwald, I. Hutchinson, J. Irby, Y. Lin, A. Mazurenko, and M. Porkolab, Plasma Phys. Controlled Fusion **43**, L23 (2001).

[9]A. Mazurenko, M. Porkolab, D. Mossessian, J. Snipes, X. Xu, and W. Nevins, Phys. Rev. Lett. **89**, 225004, 1 (2002).

[10]J. Terry, N. Basse, I. Cziegler, M. Greenwald, O. Grulke, B. LaBombard, S. Zweben, E. Edlund, J. Hughes, L. Lin, Y. Lin, M. Porkolab, M. Sampsell, B. Veto, and S. Wukitch, Nucl. Fusion **45**, 1321 (Oct 2005).

[11]LaBombard, B. and Golfinopoulos, T. and Terry, J.L. and Brunner, D. and Davis, E. and Greenwald, M. and Hughes, J.W. and the Alcator C-Mod Team, Phys. Plasmas(2014-accepted).

[12]I. H. Hutchinson, R. Boivin, F. Bombarda, P. Bonoli, S. Fairfax, C. Fiore, J. Goetz, S. Golovato, R. Granetz, M. Greenwald, S. Horne, A. Hubbard, J. Irby, B. LaBombard, B. Lipschultz, E. Marmar, G. McCracken, M. Porkolab, J. Rice, J. Snipes, Y. Takase, J. Terry, S. Wolfe, C. Christensen, D. Garnier, M. Graf, T. Hsu, T. Luke, M. May,

A. Niemczewski, G. Tinios, J. Schachter, and J. Urbahn, Phys. Plasmas (1994-present) **1**, 1511 (1994).

[13]K. V. Roberts and J. B. Taylor, Phys. Rev. Lett. **8**, 197 (Mar 1962).

[14]A. Galeev and V. Oraevskiĭ, Soviet Physics JETP **17**, 615 (Mar 1963).

[15]S. Moiseev and R. Sagdeev, Soviet Physics JETP-USSR **17**, 515 (1963), ISSN 0038-5646.

[16]A. Mikhaĭlovskiĭ and L. Rudakov, Soviet Physics JETP **17**, 621 (Mar 1963).

[17]M. N. Rosenbluth and A. Simon, Physics of Fluids **8**, 1300 (1965).

[18]B. Coppi, G. Laval, R. Pellat, and M. Rosenbluth, Nucl. Fusion **6**, 261 (1966).

[19]K. Kitao, Plasma Physics **9**, 523 (1971).

[20]N. A. Krall, in *Advances in Plasma Physics*, Vol. 1, edited by A. Simon and W. B. Thompson (Interscience Publishers, John Wiley and Sons, 1968) pp. 153–199.

[21]F. Hinton and C. Horton, Physics of Fluids **14**, 116 (Jan 1971).

[22]A. Mosetto, D. H. Federico, S. Jolliet, and P. Ricci, Phys. Plasmas **19**, 112103 1 (2012).

[23]B. D. Scott, Physics of Fluids B: Plasma Physics **4**, 2468 (1992).

[24]B. Scott, *Low Frequency Fluid Drift Turbulence in Magnetised Plasmas* (Max-Planck-Institut für Plasmaphysik Research Report: IPP 5/92, 2001).

[25]A. Kendl and B. D. Scott, Phys. Rev. Lett. **90**, 035006 (Jan 2003).

[26]B. LaBombard, J. Hughes, D. Mossessian, M. Greenwald, B. Lipschultz, J. Terry, and the Alcator C-Mod Team, Nucl. Fusion **45**, 1658 (2005).

[27]Y. Lin, *Experimental Application and Numerical Study of Reflectometry in the Alcator C-Mod Tokamak*, Ph.D. thesis, Massachusetts Institute of Technology (2001).

[28]M. B. Sampsell, *Beam Emission Spectroscopy on the Alcator C-Mod Tokamak*, Ph.D. thesis, University of Texas at Austin (2004).

[29]T. Uckan, B. Richards, A. Wooton, R. D. Bengston, R. Bravenec, B. Carreras, G. Li, P. Hurwitz, P. Phillips, W. Rowan, H. Tsui, J. Uglum, Y. Wen, and D. Winslow, Journal of Nuclear Materials **220-22**, 663 (1996).

[30]K. Zhai, Y.-Z. Wen, C.-X. Yu, W.-D. Liu, S.-D. Wan, G. Zhuang, W. Yu, and Z.-Z. Xu, Nucl. Fusion **37**, 1709 (1997).

[31]C. Schröder, T. Klinger, D. Block, A. Piel, G. Bonhomme, and V. Naulin, Phys. Rev. Lett. **86**, 5711 (Jun 2001).

[32]C. Brandt, O. Grulke, and T. Klinger, Phys. Plasmas (1994-present) **17**, 032304 (2010).

[33]C. Brandt, O. Grulke, and T. Klinger, Plasma Phys. Control. Fusion **52**, 055009 (2010).

[34]G. G. Borg and R. C. Cross, Plasma Phys. Control. Fusion **29**, 681 (1987).

[35]J. Goedbloed, H. Holties, S. Poedts, G. Huymans, and W. Kerner, Plasma Phys. Control. Fusion **35**, B277 (1993).

[36]A. Fasoli, D. Borba, G. Bosia, D. J. Campbell, J. A. Dobbing, C. Gormezano, J. Jacquinot, P. Lavanchy, J. B. Lister, P. Marmillod, J.-M. Moret, A. Santagiustina, and S. Sharapov, Phys. Rev. Lett. **75**, 645 (Jul 1995).

[37]A. Fasoli, J. Dobbing, C. Gormezano, J. Jacquinot, J. Lister, S. Sharapov, and A. Sibley, Nucl. Fusion **36**, 258 (1996).

[38]A. Fasoli, D. Borba, C. Gormezano, R. Heeter, A. Jaun, J. Jacquinot, W. Kerner, Q. King, J. Lister, S. Sharapov, D. Start, and L. Villard, Plasma Phys. Control. Fusion **39**, B287 (1997).

[39]A. Fasoli, D. Testa, S. Sharapov, H. Berk, B. Breizman, A. Gondhalekar, R. Heeter, M. Mantsinen, and contributors to the EFDA-JET Workprogramme, Plasma Phys. Control. Fusion **44**, B159 (2002).

[40]Panis, Theodore and Testa, D. and Fasoli, A. and Klein, A. and Carfantan, H. and Blanchard, P. and JET-EFDA Contributors, Nucl. Fusion **50**, 1 (Jul 2010).

[41]D. A. Schmittdiel, *Investigation of Alfvén Eigenmodes in Alcator C-Mod Using Active MHD Spectroscopy*, Master's project, Massachusetts Institute of Technology, Nuclear Engineering Department (2003).

[42]J. Snipes, N. Basse, C. Boswell, E. Edlund, A. Fasoli, N. Gorelenkov, R. Granetz, L. Lin, Y. Lin, R. Parker, M. Porkolab, J. Sears, S. Sharapov, V. Tang, and S. Wukitch, Phys. Plasmas **12**, 056102 (2005).

[43]J. Sears, *Measurement and Interpretation of Stable and Unstable Alfvén Eigenmodes in the Presence of Fast Ions in Alcator C-Mod*, Ph.D. thesis, MIT (2010).

[44]J. Sears, R. Parker, J. Snipes, T. Golfinopoulos, A. Bader, G. Kramer, and V. Tang, Nucl. Fusion **52**, 083003 (2012).

[45]Plansee, "Report 530 DE 05.04 (3000) RWF: Molybdenum: Material Properties and Applications," Tech. Rep. (Plansee, 2004), `www.plansee.com/pdfs/Molybdenum.pdf`.

[46]A more precise analysis of the vacuum field perturbation will be given elsewhere[63].

[47]D. Whyte, A. Hubbard, J. Hughes, B. Lipschultz, J. Rice, E. Marmar, M. Greenwald, I. Cziegler, A. Dominguez, T. Golfinopoulos, N. Howard, L. Lin, R. McDermott, M. Porkolab, M. Reinke, J. Terry, N. Tsujii, S. Wolfe, S. Wukitch, Y. Lin, and the Alcator C-

Mod Team, Nucl. Fusion **50**, 105005 (2010).

[48]T. Golfinopoulos, B. LaBombard, W. Burke, R. R. Parker, W. Parkin, and P. Woskov, Rev. Sci. Instrum.(2014-submitted).

[49]A. Mazurenko, *Phase Contrast Imaging on the Alcator C-Mod tokamak*, Ph.D. thesis, Massachusetts Institute of Technology (Sep 2001).

[50]W. F. Bergerson, P. Xu, J. Irby, D. Brower, W. Ding, and E. Marmar, Rev. Sci. Instrum. **83** (2012).

[51]R. Fisher and R. Gould, Phys. of Fluids **14**, 857 (Apr. 1971).

[52]R. R. Parker and R. Briggs, MIT Res. Lab. Electronics Quarterly Prog. Report **104** (1972).

[53]P. M. Bellan and M. Porkolab, Physics of Fluids (1958-1988) **17** (1974).

[54]H. H. Kuehl, Physics of Fluids (1958-1988) **17** (1974).

[55]M. Ono, Phys. Rev. Lett. **42**, 1267 (May 1979).

[56]T. H. Stix, *Waves in Plasmas* (American Institute of Physics, 1997) ISBN 0883188597.

[57]Ion-ion collisions are stabilizing for drift waves, but the ion-ion collision time is $\tau_{ii} \approx 5\ \mu$s, so that $\tau_{ii}^{-1}/\omega \approx 0.3$.

[58]B. Dudson, M. Umansky, X. Xu, P. Snyder, and H. Wilson, Computer Physics Comm. **180**, 1467 (2009).

[59]The outer 21 chords are selected from the full set of 32 because they reliably show a strong coherent signal with the antenna across a number of discharges. Not all of the inner PCI chords map to the antenna, as shown, for example, in Figure 11, and also the inner chords suffer greater attenuation in coherent signal because they map to points with increased gap between the antenna and the LCFS.

[60]Extrapolating $\tilde{B}_\theta$ to the LCFS requires scaling by a factor $\sim 10^2$ that is very sensitive to the spacing between the LCFS and the wall-mounted coil.

[61]In particular, simultaneous, co-located fluctuations measurements and background profiles of plasma potential, electron density, and electron temperature.

[62]E. Davis, M. Porkolab, J. Hughes, B. LaBombard, P. Snyder, and X. Xu, APS DPP Meeting(Nov. 2013), `http://meetings.aps.org/link/BAPS.2013.DPP.PP8.17`.

[63]T. Golfinopoulos, Ph.D. thesis, Massachusetts Institute of Technology (2014-to be submitted).